

Numerical Simulation of the Gulf Stream and Mid-Ocean Eddies

ALBERT J. SEMTNER, JR.¹, AND YALE MINTZ

Department of Atmospheric Sciences, University of California, Los Angeles 90024

(Manuscript received 26 July 1976, in revised form 6 December 1976)

ABSTRACT

The circulation of the western North Atlantic is simulated with a primitive equation model that has 5 levels and a horizontal grid size of 37 km. The idealized model domain is a rectangular basin, 3000 km long, 2000 km wide and 4 km deep, which is oriented so that the long axis of the basin is parallel to the east coast of the United States. The nearshore side of the basin has a simple continental shelf and slope, whereas the other sides are bounded by vertical walls. The model ocean is driven by a $2\frac{1}{2}$ gyre pattern of steady zonal wind stress and by a Newtonian-type surface heating. After initialization from a 15-year spin-up with a coarser grid, two experiments are carried out, each of several years duration: the first uses a Laplacian formulation for the subgrid-scale lateral diffusions of heat and momentum, the second uses a highly scale-selective biharmonic formulation for these diffusions. Bottom friction is present in each case.

In both experiments, a western boundary current forms which separates from the coast and continues eastward as an intense free jet, with surface velocities $>1 \text{ m s}^{-1}$ for almost 1000 km downstream. In the experiment with biharmonic closure, this simulated Gulf Stream develops large-amplitude transient meanders, some of which become cold-core cyclonic rings and warm-core anticyclonic rings that drift westward. In both experiments, transient mesoscale eddies also form in the broad westward-moving North Equatorial Current, where the simulated thermocline in the model ocean slopes downward toward the north. The remaining regions of the model ocean also contain transient mesoscale eddies, but they are of weaker intensity.

The dominant process of eddy kinetic energy production, in both experiments, is a baroclinic-barotropic instability which is concentrated in the part of the Gulf Stream that is over the continental slope. But where the Gulf Stream lies over the abyssal plains, there is a large reconversion of eddy kinetic energy into the kinetic energy of the time-averaged flow. Eddy kinetic energy is also produced by baroclinic instability in the North Equatorial Current, but at a much smaller rate. In the biharmonic experiment, the eddies transfer considerable kinetic energy downward, and bottom friction is the dominant process of eddy kinetic energy dissipation.

An analysis of the heat transport, in the biharmonic experiment, shows that the horizontal transport of heat by eddies is much larger than the subgrid-scale horizontal heat diffusion. In the Gulf Stream region, the eddy heat transport is comparable to the effect of a lateral diffusion coefficient of $10^7 \text{ cm}^2 \text{ s}^{-1}$.

1. Introduction

Over the past 15 years, oceanographic field measurements have disclosed the existence of intense, transient mesoscale motions in many parts of the world ocean. This revelation that the circulation in the ocean interior is not a weak, quasi-steady planetary-scale phenomenon, as previously thought, has provided new challenges to the oceanographic community, and has led to large national and multinational observing programs, such as the USSR POLYGON experiment (Koshlyakov and Grachev, 1973), the U. S. MODE-I experiment (MODE-I Dynamics Group, 1975), and the joint POLYMODE program (Joint POLYMODE Working Groups, 1976).

To help understand the dynamics of the eddies and the role they may play in the general circulation of the

oceans, a number of supplementary numerical modelling efforts have been undertaken. Some of these studies have been carried out with respect to local eddy dynamics, either in the mid-ocean (e.g., Rhines, 1976; Owens and Bretherton, 1977; Huppert and Bryan, 1976) or in the western boundary current (Orlanski and Cox, 1973). Others have dealt with the interactions between the mesoscale eddies and the large-scale circulation in closed ocean basins, using sufficient resolution to represent the mesoscale eddies explicitly. The first experiments in this category have been made with an adiabatic two-layer primitive equation model (Holland and Lin, 1975) or with adiabatic quasi-geostrophic models (Holland, 1977; Haidvogel, 1976). The present study uses a diabatic multilevel primitive-equation model. This allows us to investigate the spontaneous generation of transient mesoscale eddies and their interactions with the large-scale circulation within the model ocean as a consequence of external large-

¹ Present affiliation: National Center for Atmospheric Research, Boulder, Colo. 80303.

scale thermal forcing as well as wind forcing. The model has been used in two previous studies with flat-bottomed basins (Robinson *et al.*, 1977; Han, 1975), but it is generalized here to include bottom topography in the form of a simple continental shelf and slope.

2. Governing equations and boundary conditions

The governing equations of the model are

$$\frac{\partial \mathbf{v}}{\partial t} + \mathbf{v} \cdot \nabla \mathbf{v} + w \frac{\partial \mathbf{v}}{\partial z} + f(\mathbf{k} \times \mathbf{v}) = -\frac{1}{\rho_0} \nabla p + \kappa \frac{\partial^2 \mathbf{v}}{\partial z^2} \begin{cases} +A_M \nabla^2 \mathbf{v} \\ \text{or} \\ -B_M \nabla^4 \mathbf{v} \end{cases} \quad (1)$$

$$\frac{\partial p}{\partial z} = -\rho g \quad (2)$$

$$\nabla \cdot \mathbf{v} + \frac{\partial w}{\partial z} = 0 \quad (3)$$

$$\frac{\partial T}{\partial t} + \mathbf{v} \cdot \nabla T + w \frac{\partial T}{\partial z} = \frac{\kappa}{\delta} \frac{\partial^2 T}{\partial z^2} \begin{cases} +A_H \nabla^2 T \text{ (Laplacian closure)} \\ \text{or} \\ -B_H \nabla^4 T \text{ (biharmonic closure)} \end{cases} \quad (4)$$

$$\rho = \rho_0 [1 - \alpha(T - T_0)] \quad (5)$$

$$\delta = \begin{cases} 1, & \partial T / \partial z \geq 0 \\ 0, & \partial T / \partial z < 0. \end{cases} \quad (6)$$

Here \mathbf{v} , w , p , T and ρ represent horizontal velocity, vertical velocity, pressure, temperature and density. The ∇ operator applies to horizontal variations only. Other symbols have their usual meanings. The usual simplifications, in the form of the hydrostatic approximation, the incompressibility condition and a linearized equation of state, have reduced the problem to one of predicting horizontal motion and temperature with two conservation equations. In these equations, the vertical mixing by subgrid-scale processes is taken to behave like enlarged molecular diffusion, except when gravitational instability occurs. In that event, convective adjustment is used to instantaneously restore neutral stability (symbolized above as the case $\delta=0$). Horizontal mixing by subgrid-scale turbulence is assumed to occur in one of two ways. In one experiment, a molecular-type Laplacian diffusion operator is used and in the other a highly scale selective biharmonic operator is employed. (The use of a biharmonic operator was suggested by W. R. Holland, on the basis of his experience with it in two-layer quasi-geostrophic experiments.)

The Laplacian closure hypothesis for subgrid-scale turbulent mixing has been used in so many numerical experiments in the past that there is a tendency to forget its *ad hoc* character. Recent observational and theoretical evidence suggests that a more scale-selective mixing of momentum may occur in the atmosphere and oceans. Tokioka (1977) has developed a numerical formulation of quasi-geostrophic turbulent mixing, in which the spatial form of the operator is biharmonic. Tokioka's method has a variable viscosity coefficient; but this refinement may not matter if the spatial operator reduces the lateral damping of the flow so that bottom friction assumes a major role in energy dissipation.

The value of A_H which we are forced to use in the Laplacian experiment may be somewhat high, relative to what occurs in nature. This value of A_H could not be chosen arbitrarily small, for the given grid size, because computational noise arises if A_H is below a critical value (Chen, 1971). However, by using a biharmonic operator, a value of B_H can be chosen to give the same control of computational noise, while drastically cutting down the diffusion of features having mesoscale wavelength. In this way, unrealistic damping is reduced, except for features which are poorly resolved anyway; and advective effects are enhanced for the larger-scale phenomena.

The governing equations are solved within the domain shown in Fig. 1 and with the bottom topography shown in Fig. 2. A profile of the prescribed zonal wind stress is also shown in Fig. 1. This geometry and wind forcing was chosen as a suitable extension of two previous eddy-resolving experiments. The experiment of Robinson *et al.* (1977) was for a 2000 km \times 2000 km flat-bottom ocean, with a single-gyre anticyclonic wind forcing, and produced a strong boundary current along its northern wall and transient mesoscale eddies in the ocean interior. However, the instability properties of a boundary current at a northern wall have been shown by Holland and Lin (1975) to differ from those of a free interior jet. Therefore, in the experiment of Han (1975), the possibility of a free interior jet was allowed by the addition of a northern half-gyre of cyclonic wind forcing. But, as Fig. 3 shows, the western boundary current separates from the coast north of the latitude of zero wind stress curl and flows southward parallel to the coast. This pattern does not resemble the way in which the observed Gulf Stream separates from the coast south of the latitude of zero wind stress curl and then flows east-northeastward. It is because the orientation of the coastline and the presence of a continental slope may influence the point of separation and the direction in which the current flows after leaving the coast, that the present geometry was chosen. A fully two-dimensional bottom topography would make the model basin even more realistic, but that would more than double the computing time required (cf. Section 3).

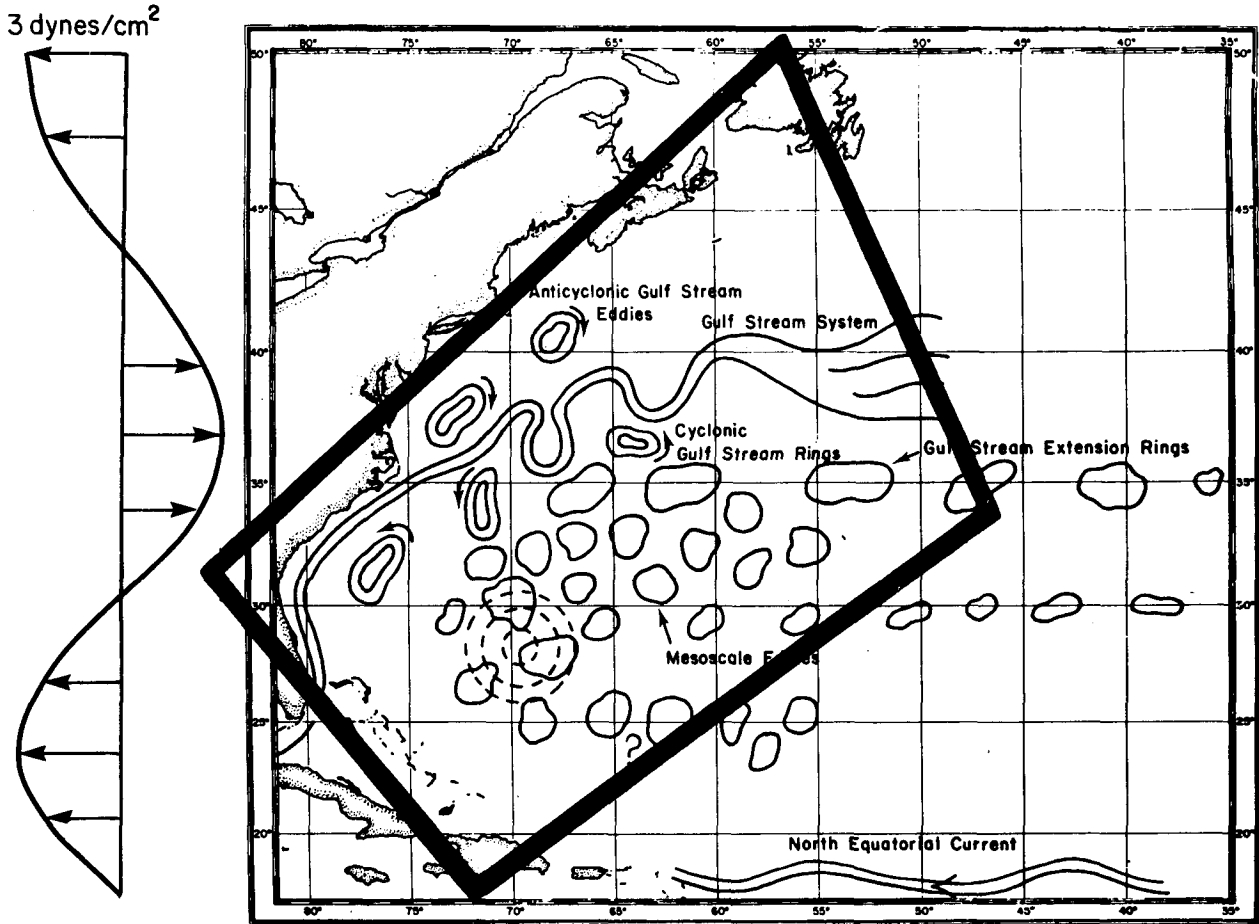


FIG. 1. The boundary of the model domain, superimposed on a schematic picture of mesoscale variability in the western portion of the North Atlantic (Joint POLYMODE Working Groups, 1976). Also shown is the zonal wind stress which drives the model ocean.

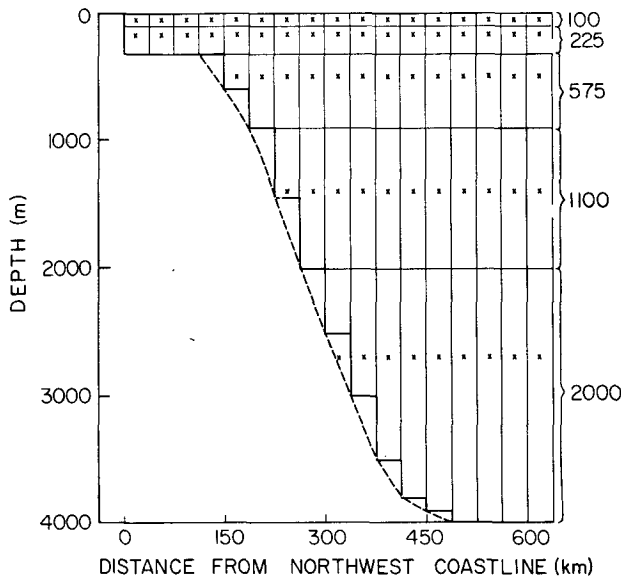


FIG. 2. Model topography and grid box placement near the northwest coastline. A smoothly varying representation of the continental slope (dashed line) is made possible by varying the grid box thickness near the slope.

Since the east-west dimension of the model, at the latitude of maximum anticyclonic wind stress curl, is only about one-third the width of the subtropical North Atlantic, the amplitude of the zonal wind stress is taken as $3 \times 1 \text{ dyn cm}^{-2}$. In this way, the linear component of the western boundary current will have the correct magnitude.

The boundary conditions for the present study are as follows:

- 1) The rigid-lid assumption ($w=0$ at $z=0$), which allows a longer time step than in a free-surface model by filtering out surface gravity waves.
- 2) No flow through the lower boundary ($w = -\mathbf{v} \cdot \nabla H$, at $z = -H$); and no flow through the lateral boundaries.
- 3) A prescribed zonally constant surface stress as shown in Fig. 1.
- 4) Quadratic bottom stress, following Weatherly (1972):

$$\tau^b = (1.3 \times 10^{-3}) \rho_0 (u^2 + v^2)^{1/2} (u \cos 10^\circ - v \sin 10^\circ, u \sin 10^\circ + v \cos 10^\circ). \quad (7)$$

- 5) A free-slip condition at the lateral boundaries. This is done to reduce dissipation by lateral friction

and let the structure of the boundary currents be determined mainly by bottom friction. Blandford (1971) has shown that the use of a free-slip condition has this effect.

6) Following Haney (1974), a heat flux through the upper boundary which is proportional to the difference between the calculated ocean surface temperature T_s and a prescribed atmospheric reference temperature T^A . (In the present experiment, T^A varies linearly from 0°C at 50°N to 30°C at 18°N , and the constant of proportionality γ is $60 \text{ cal cm}^{-2} \text{ day}^{-1} (^\circ\text{C})^{-1}$.)

7) No heat flux through the lateral boundaries and no heat flux through the lower boundary.

3. Description of the numerical model

The numerical model was designed for the present experiments by the first author of this paper. It is the model that was also used by Robinson *et al.* (1977) and by Han (1975). It has a number of features which are improvements on previous ocean models. These are (i) a finite-difference scheme which conserves mean-square vorticity, as well as mass, momentum, and energy; (ii) a variable thickness for the lowermost grid boxes, to permit better resolution of bottom topography without increasing the number of vertical levels; (iii) a fast non-iterative method for obtaining the transport streamfunction when topography varies only in one coordinate direction; and (iv) coding that takes advantage of the array-processing design of the IBM 360/91 (cf. Anderson *et al.*, 1967) and thereby reduces the computing time by a factor of 3.

A staggered arrangement of gridpoints is chosen, with u and v defined at one set of points and T and p at another. This placement of gridpoints has been shown by Arakawa (1972) to give a superior representation of the geostrophic adjustment process. Its main drawback is that diagonally oriented two-gridpoint waves have zero phase speed. However, such "checkerboard noise" does not interact strongly with the model physics. Its effect is automatically removed from most terms in the finite-difference equations by means of averaging operators.

The lateral boundaries of the grid lie on the temperature points. This differs from some previous models (e.g., Bryan, 1969; Semtner, 1974), where the location of the boundary on velocity points permits a simpler numerical formulation, but does not guarantee momentum conservation at the boundary. Furthermore, to conserve kinetic energy in those models, a no-slip boundary condition must be used for the advection terms. We place the boundary on the temperature points (as in Haney, 1974) in order to avoid lateral momentum leaks, which could distort the highly nonlinear circulation. It then becomes possible to use a free-slip boundary condition, so that bottom friction can be the dominant process for energy dissipation.

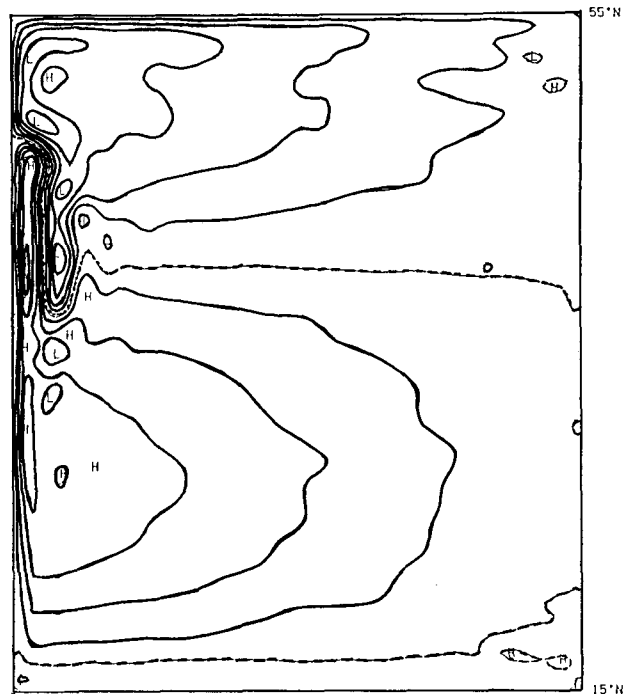


FIG. 3. The transport streamfunction for the time-averaged flow in the experiment of Han (1975). Contour interval is $10^7 \text{ m}^2 \text{ s}^{-1}$.

The domain shown in Fig. 1 is a portion of a spherical coordinate system whose equator runs from southwest to northeast through the center of the region. With a horizontal grid size of 0.3375° in the latitude φ and longitude λ of the coordinate system, the domain becomes a 54×80 array of grid boxes, each approximately 37 km on a side. At each location, up to five momentum grid boxes are stacked downward until the bottom is reached (see Fig. 2). A variable thickness of the bottom box gives reasonable resolution of the continental slope. Momentum gridpoints, indicated by x's in Fig. 2, are arranged in the vertical so that points on opposite sides of an interface are equidistant from that interface (as in Haney, 1974). Temperature gridpoints (not shown) are located on the corners of the momentum grid boxes, at the same depth as the corresponding momentum gridpoints.

Finite-difference equations, having second-order accuracy in the grid size Δs , are developed by considering budgets for the various momentum boxes and subsidiary temperature boxes. Rather than present the general equations, which permit fluxes across different sized box faces near the continental slope, we will give the equations for the flat portion of the domain first, and indicate later how they are modified for topography. To keep the equations relatively compact, index-free averaging and finite-difference operators will be employed. {For example, $\delta_\lambda u = [u(\lambda + \Delta\lambda/2) - u(\lambda - \Delta\lambda/2)]/\Delta\lambda$ and $\bar{u}^\lambda = [u(\lambda + \Delta\lambda/2) + u(\lambda - \Delta\lambda/2)]/2$.}

The finite-difference momentum equation for the u

component, in the case of Laplacian friction, is

$$\begin{aligned}
 \delta_t u + \frac{2}{3a \cos \varphi} \{ \delta_{\lambda} [\bar{u}^{\varphi} \bar{u}^{\lambda}] + \delta_{\varphi} [(\cos \varphi \bar{v})^{\varphi} \bar{u}^{\lambda}] \} \\
 + \frac{1}{3\sqrt{2}a \cos \varphi} \{ \delta_{\lambda'} [(\cos \varphi \bar{v})^{\varphi} \bar{u}^{\lambda'}] + \delta_{\lambda} [\bar{u}^{\varphi} \bar{u}^{\lambda'}] \} \\
 + \frac{1}{3\sqrt{2}a \cos \varphi} \{ \delta_{\varphi'} [(\cos \varphi \bar{v})^{\varphi} \bar{u}^{\varphi'}] - \delta_{\varphi} [\bar{u}^{\varphi} \bar{u}^{\varphi'}] \} \\
 + \delta_z (\bar{w}^z) - \frac{\tan \varphi}{a} uv - fv = -\frac{1}{\rho_0 a \cos \varphi} \delta_{\lambda} (\bar{p}^{\varphi}) + \kappa \delta_z (\delta_z u) \\
 + A_M \left\{ \frac{1}{a^2 \cos^2 \varphi} \delta_{\lambda} (\delta_{\lambda} u) + \frac{1}{a^2 \cos \varphi} \delta_{\varphi} (\cos \varphi \delta_{\varphi} u) \right\}. \quad (8)
 \end{aligned}$$

Symbols λ' and φ' refer to diagonal coordinate directions given by the change of variables $\lambda' = \varphi + \lambda$ and $\varphi' = \varphi - \lambda$. The radius of the earth is a and the Coriolis parameter (which depends on both φ and λ) is f .

Except for the horizontal advection terms, the finite-difference equation is a straightforward representation of the original differential equation. The time extrapolation is normally carried out in a leapfrog fashion for advective, Coriolis and pressure gradient terms, and in a forward fashion for diffusive terms. To avoid the separation of solutions associated with the leapfrog timestep, the non-diffusive terms are integrated every tenth timestep with an Euler-backward scheme. This has been found to be superior to the use of a simple forward timestep in controlling solution separation and in damping high-frequency noise.

The momentum advection terms follow the formulation in the UCLA atmospheric model having the same horizontal gridpoint arrangement (Arakawa, 1972). In atmospheric simulations, this formulation prevents much of the buildup of computational noise that occurs with simpler schemes. The method is based on analogy with the Arakawa (1966) scheme for vorticity advection, whereby each gridpoint exchanges vorticity with all eight gridpoints around it, using velocities suitably defined between each pair of gridpoints. Arakawa's (1966) method prevents a false cascade of energy into high wavenumbers, because it formally conserves both kinetic energy and mean square vorticity. In the momentum formulation there is no formal guarantee that mean square vorticity will be conserved (on account of the averaging operators involved); but an empirical comparison of the vorticity advection and momentum advection schemes in a barotropic ocean model (Lee, 1976) has shown the two schemes to be nearly identical.

Boundary conditions for horizontal momentum advection are set by reflecting the tangential velocity components and the negatives of the normal velocity components outside the margin of the grid. All averaging

and difference operations are carried out as usual for gridpoints next to the wall, except that whenever a diagonal averaging operation would cross the grid boundary, it is changed to be an average inside the boundary and parallel to it. (This minor change gives a formal guarantee that both energy and momentum will be fully conserved.) These boundary conditions have been compared with the analogous free-slip boundary condition on vorticity ($\zeta=0$) in a barotropic model and found to give nearly identical results (Lee, 1976).

The v momentum equation has a finite-difference form analogous to that of the u equation, and need not be exhibited. To obtain a continuity equation for momentum boxes, one applies the Arakawa formulation of horizontal advection to the scalar field $\theta \equiv 1$ and equates the results to $-\delta_z w$. This determines w at each interface between boxes in a vertical column (starting from $w=0$ at the surface). It can be shown that w vanishes at the bottom of a flat ocean, so that total mass is conserved by this finite-difference scheme. Total mass is also conserved in the case with bottom topography, as will be shown later.

The temperature prediction equation with Laplacian diffusion is relatively straightforward:

$$\begin{aligned}
 \delta_t T + \frac{1}{a \cos \varphi} [\delta_{\lambda} (\bar{u}^{\varphi} \bar{T}^{\lambda}) + \delta_{\varphi} (\cos \varphi \bar{v}^{\varphi} \bar{T}^{\lambda})] + \delta_z (\bar{w}^z \bar{T}^z) \\
 = \kappa \delta_z (\delta_z T) + A_H \left[\frac{1}{a^2 \cos^2 \varphi} \delta_{\lambda} (\delta_{\lambda} T) \right. \\
 \left. + \frac{1}{a^2 \cos \varphi} \delta_{\varphi} (\cos \varphi \delta_{\varphi} T) \right]. \quad (9)
 \end{aligned}$$

The treatment of time-marching is the same as in the momentum equations, except that after each timestep any pair of gravitationally unstable layers are mixed together. To predict temperature at a point on the lateral boundary, the above equation can still be used, provided that temperature values one gridpoint inside the boundary are reflected across the wall, and provided that u and v image values are defined as for the momentum equations. In this way, the fact that the temperature boxes on the boundary are only half-boxes (or quarter-boxes at the corners) is correctly taken into account.

A continuity equation for temperature boxes is obtained by putting $T \equiv 1$ in (9). The w values obtained by downward integration in vertical temperature columns are related to the w values in momentum columns by a four-point horizontal averaging operation. Also $w=0$ at the bottom, and mass is again conserved.

The finite-difference form of the hydrostatic relation can be combined with the equation of state to yield

$$\delta_z \bar{p}^* = g \rho_0 \alpha (\bar{T}^z - T_0), \quad (10)$$

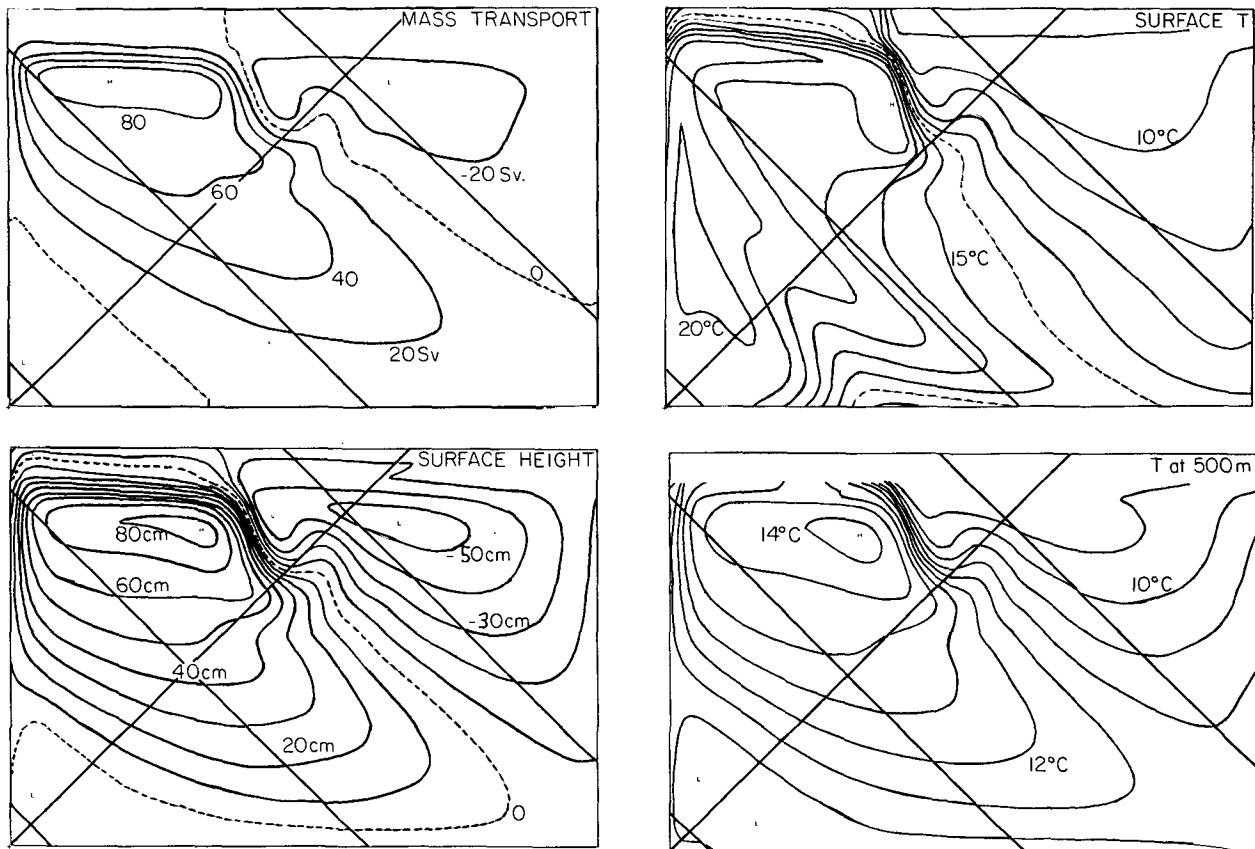


FIG. 4. The steady predicted fields obtained from a $15\frac{1}{2}$ year integration with $A_M = A_H = 10^7 \text{ cm}^2 \text{ s}^{-1}$.

where p^* is the pressure anomaly due to deviations of T from T_0 . (T_0 is taken to be 5°C in these calculations.) The model makes use of p^* rather than p in the momentum equations to reduce machine truncation errors in the calculation of horizontal pressure gradient forces. The form of the hydrostatic relation is such that no fictitious energy source exists in conversions between potential energy and kinetic energy by buoyancy forces.

The finite-difference form of the biharmonic operator in both the momentum and heat equations is simply $\bar{\nabla}^2 \bar{\nabla}^2$, where

$$\bar{\nabla}^2(\cdot) = -\frac{1}{a^2 \cos^2 \varphi} \delta_\lambda [\delta_\lambda(\cdot)] + \frac{1}{a^2 \cos \varphi} \delta_\varphi [\cos \varphi \delta_\varphi(\cdot)]. \quad (11)$$

Boundary conditions for temperature prediction are set by taking the values of T and of $\bar{\nabla}^2 T$ which are defined one gridpoint inside the wall and reflecting them through the boundary. It can be shown that this choice conserves heat in exchanges between gridpoints and prevents heat transfer through the boundary. The fractional area of the boxes along the wall is also taken into account. For the momentum equations, the proper boundary conditions to prevent momentum exchange across the wall consist in reflecting the values of \mathbf{v} and of $\bar{\nabla}^2 \mathbf{v}$ across the boundary.

The scale selectivity of the biharmonic operator over the Laplacian operator can be illustrated by inserting a waveform

$$T(x, y, t) = c(t) e^{i(kx + ly)}$$

into the Cartesian forms of the finite difference equations

$$\frac{\partial T}{\partial t} = A \bar{\nabla}^2 T,$$

$$\frac{\partial T}{\partial t} = -B \bar{\nabla}^2 \bar{\nabla}^2 T.$$

In the first instance, the time decay of the amplitude is

$$c(t) = \exp \left\{ -At \left[\frac{\sin^2 \frac{1}{2} k \Delta x}{(\frac{1}{2} \Delta x)^2} + \frac{\sin^2 \frac{1}{2} l \Delta y}{(\frac{1}{2} \Delta y)^2} \right] \right\},$$

while in the second case, it is

$$c(t) = \exp \left\{ -Bt \left[\frac{\sin^2 \frac{1}{2} k \Delta x}{(\frac{1}{2} \Delta x)^2} + \frac{\sin^2 \frac{1}{2} l \Delta y}{(\frac{1}{2} \Delta y)^2} \right] \right\}.$$

To obtain the same damping of the smallest resolvable wave in either coordinate direction (e.g., when $k = \pi/\Delta x$

and $l=0$), it is necessary that

$$B = \frac{1}{4}A(\Delta x)^2.$$

This relation is used to compute B_M and B_H for the biharmonic experiment, based on the values of A_M and A_H in the Laplacian experiment. For features of meso-scale wavelength, which typically span about 14 grid-points, the biharmonic closure scheme reduces the effects of lateral diffusion by approximately a factor of 50.

Certain modifications are made in the difference equations to account for the continental slope. As is evident from Fig. 2, some gridpoints can directly interact with points immediately to the northwest of them (to the left in the figure) only across a certain fraction of their gridbox thickness. Consequently, lateral advective and diffusive fluxes across a partially open box face are weighted by the fraction of open area. Across the remaining area of the box face, a non-zero mass flux is still allowed; however this flux is felt by the adjacent column of grid boxes as a *vertical motion* at the base of the column. This mass flux is computed using the usual 8-point formula involving the v component of velocity, but the image points in the land are assumed to have $v=0$. This guarantees that when the

finite-difference continuity equation is integrated downward from $z=0$ in the adjacent column, an exactly equal mass flux at the bottom (due to a non-zero w) will be obtained. This treatment can be regarded as a consistent finite-difference version of the condition that bottom flow must be tangent to the slope, i.e.,

$$w = -\mathbf{v} \cdot \nabla H \quad \text{at } z = -H.$$

This flow which parallels the bottom in the numerical grid is also allowed to transport momentum between the grid boxes involved, so that no fictitious source of momentum (or energy) can arise in the vicinity of the slope.

For temperature prediction near the continental slope, budget equations are constructed using the volume of each grid box and the area of each box face. All of the conservative properties of the differencing schemes, for both the heat and momentum equations, continue to hold in the topographic situation. The computer program for the model independently verifies that mass, kinetic energy, total energy and heat are conserved, except for small machine truncation errors. This gives reasonable assurance that the model and its program are correctly formulated.

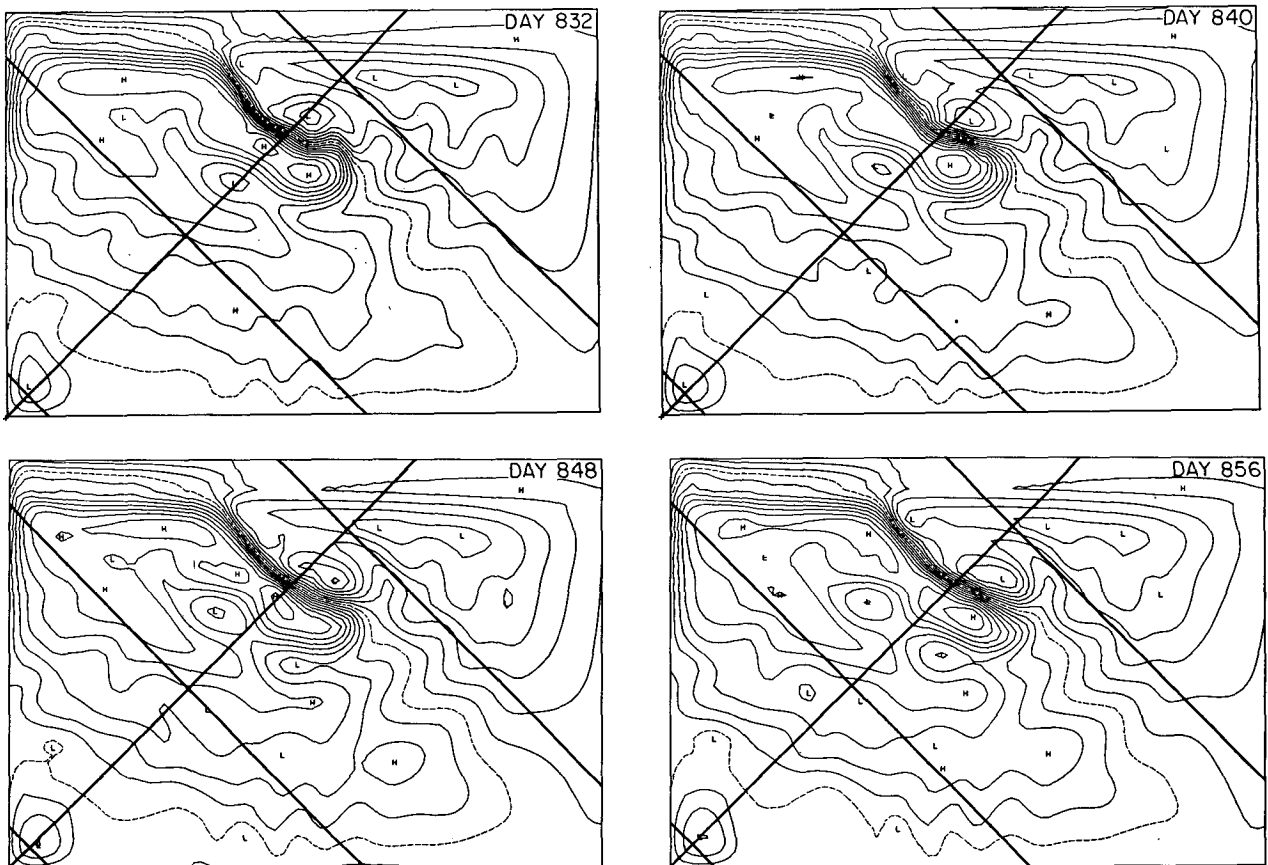


FIG. 5. Surface height fields (contour interval 10 cm) in the Laplacian experiment ($A_M = 2 \times 10^6 \text{ cm}^2 \text{ s}^{-1}$, $A_H = 6 \times 10^6 \text{ cm}^2 \text{ s}^{-1}$).

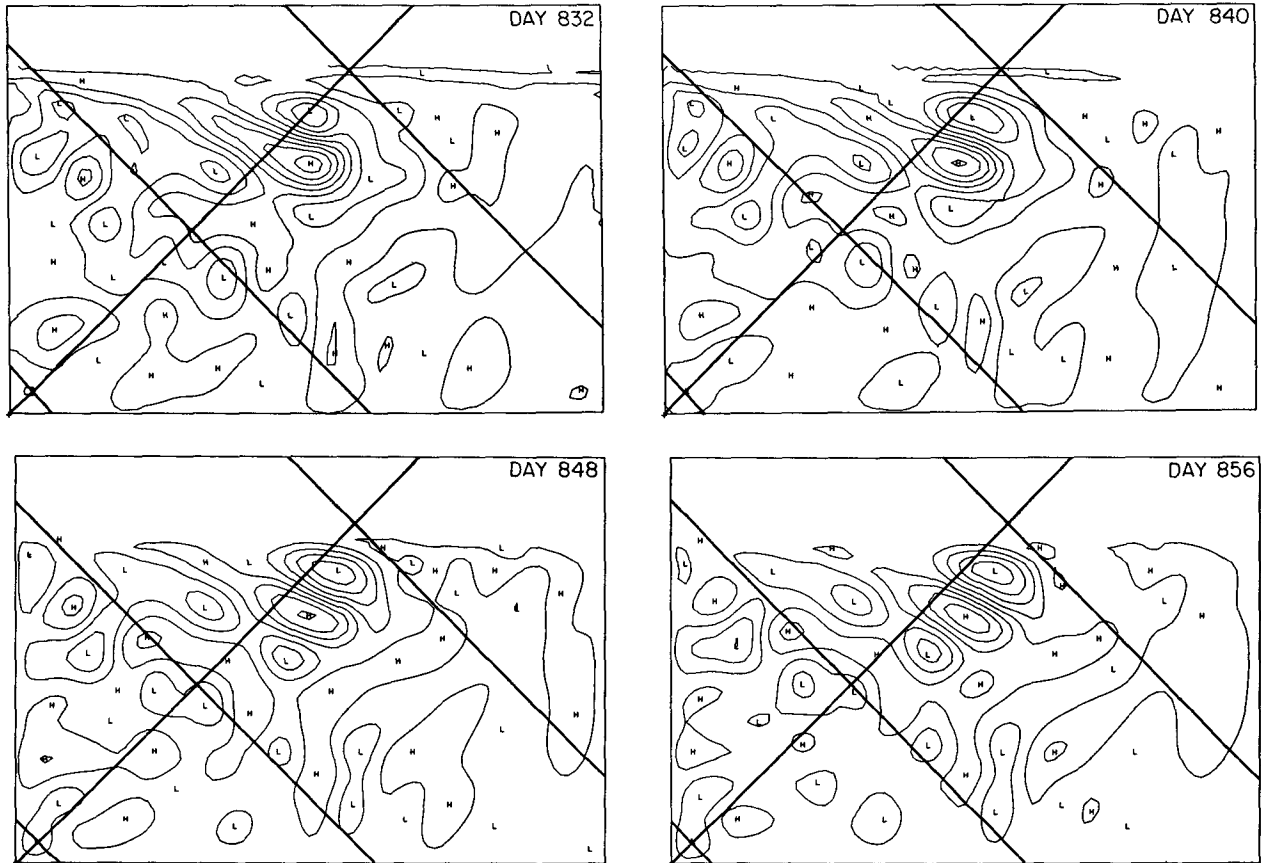


FIG. 6. Dynamic topography at 2700 db for the Laplacian experiment (5 cm contour interval).

The finite-difference momentum equation contains a pressure gradient term, through which the surface pressure $p_s = p(z=0)$ influences the flow. In rigid-lid models, no simple prediction equation for p_s exists. However, by taking the finite-difference curl of the vertically averaged vector momentum equation, a prediction equation for vorticity results, and the unknown pressure p_s does not appear. From the predicted vorticity, the streamfunction of the vertically integrated flow can be obtained by solving a Poisson-type equation. At the same time the vertical shear of the horizontal velocity can be predicted from a vertically differenced momentum equation, in which only the density dependent portion of the pressure field appears. One then combines the vertical mean flow and vertical shear flow to get the total velocity at each timestep.

The Poisson-type equation for the streamfunction ψ of the vertically integrated flow is of the form

$$\frac{1}{a \cos \varphi} \left\{ \delta_\lambda \left[\frac{1}{H a \cos \varphi} (\delta_\lambda \bar{\psi}^\varphi) \right] + \delta_\varphi \left[\frac{\cos \varphi}{H a} (\delta_\varphi \bar{\psi}^\lambda) \right] \right\} = Z. \quad (12)$$

The operator on the left-hand side can be inverted to obtain ψ only by an iterative technique, such as suc-

cessive over-relaxation (SOR). The use of such a procedure doubles the running time for the model, even when an optimal SOR parameter and very good initial guesses are employed. To avoid this, we substitute an approximate equation which can be solved by a non-iterative method for the present geometry:

$$\frac{1}{a \cos \varphi} \left\{ \delta_\lambda \left[\frac{1}{H^\varphi a \cos \varphi} \delta_\lambda \psi \right] + \delta_\varphi \left[\frac{\cos \varphi}{H^\lambda a} \delta_\varphi \psi \right] \right\} = Z. \quad (13)$$

Careful testing indicates that the solution of the above equation closely matches the solution of the original vorticity equation and that equivalent energetics are obtained with the two methods in long-term integrations. When H is independent of λ , a direct method to obtain ψ is constructed by adapting a method of Williams (1969). A trigonometric expansion of the unknown ψ in sine functions along each line of $\lambda = \text{constant}$ reduces the problem to a set of tridiagonal matrix inversions for the coefficients.

Although the surface pressure p_s is never required in the prognostic equations, it is useful to have for easy display of the nearly geostrophic flow fields. The pressure at $z=0$ can be obtained by taking line integrals of the vertically integrated equations of motion, in which

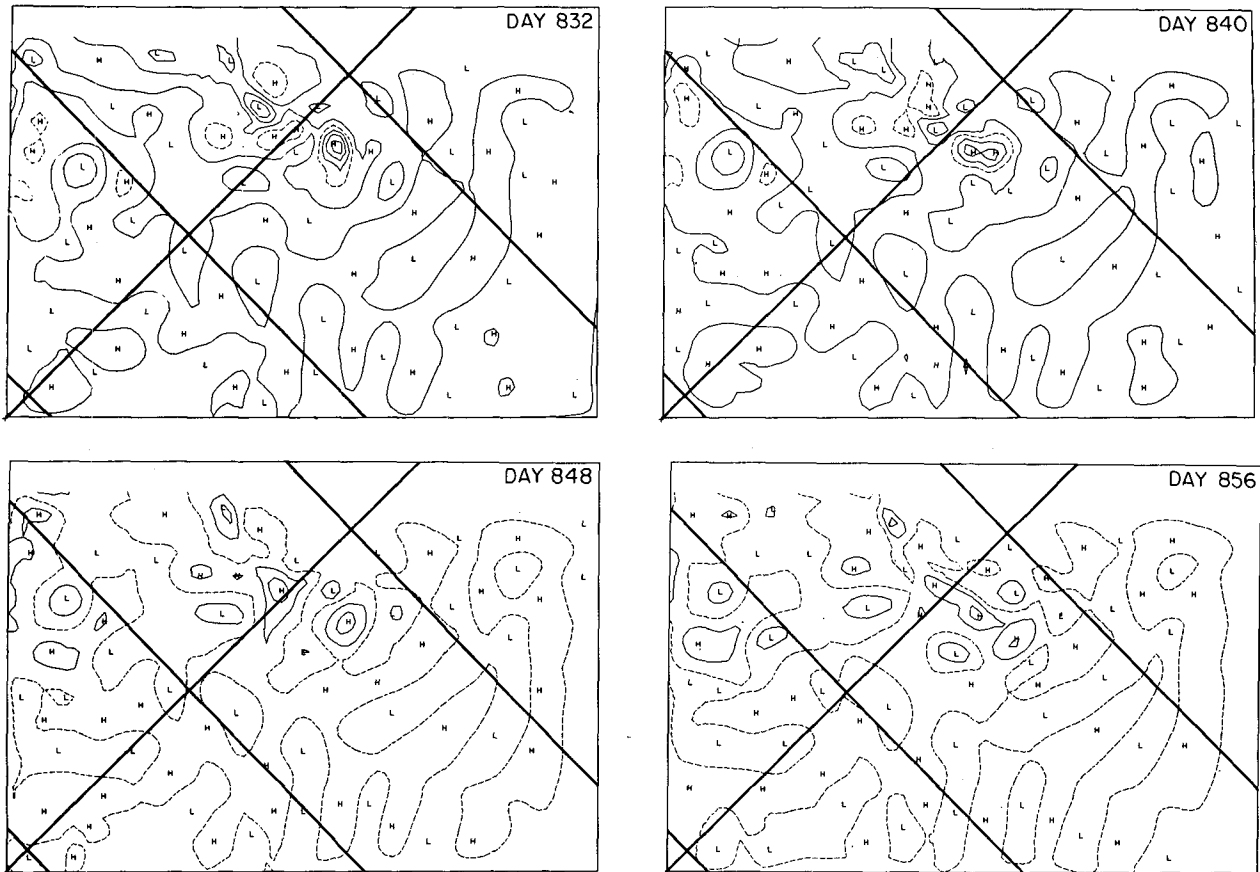


FIG. 7. Temperature deviation from time-mean values at 500 m (0.25°C contour interval).

the time derivatives are calculated from values of the streamfunction ψ . Further details on the method for computing pressure, as well as on the basic procedure for predicting the streamfunction and the vertical shear of velocity, can be found in Semtner (1974).

4. The spin-up calculation

Using the basic geometry and forcing described in Section 2, a $15\frac{1}{2}$ year spin-up was made, starting from a motionless, horizontally uniform ocean with a simple thermocline. For the first 15 years, a coarse grid with $\Delta s = 75$ km was employed. To suppress computational noise with this grid size, the values $A_M = A_H = 10^7 \text{ cm}^2 \text{ s}^{-1}$ were prescribed for the Laplacian diffusion coefficients. An interpolation was then made to the 37 km grid size, and the calculation continued for an additional half-year with the same diffusion coefficients. Mesoscale eddies did not arise in either phase of the integration.

The major reason for doing a spin-up with the coarse grid was to save computer time, but we shall see later that some interesting comparisons can be made between the results obtained with different grid sizes. Approximately 2 hours of computer time on the IBM 360/91 are required for each year of integration with

the 75 km grid, whereas 16 hours per year are needed with the 37 km grid.

In the spin-up calculation, as well as in subsequent experiments, a vertical mixing coefficient $\kappa = 1.5 \text{ cm}^2 \text{ s}^{-1}$ was used. This value may overestimate the effect of small-scale turbulent mixing, relative to that in the real ocean. If the integrations were to be carried out for many centuries, an excessively deep thermocline might develop; but for an integration period of a few decades, the effect should be negligible.

Some representative fields at the end of the $15\frac{1}{2}$ year integration with $A_M = A_H = 10^7 \text{ cm}^2 \text{ s}^{-1}$ are shown in Fig. 4. For the purpose of orientation, the geographical latitude lines at 20°N , 30°N and 40°N are included, together with the 72°W meridian.

The mass transport streamfunction exhibits a $2\frac{1}{2}$ gyre pattern, as one would expect from the wind forcing. The streamlines differs from those for a linear, flat-bottom ocean circulation in two respects: 1) the subtropical western boundary current is concentrated in the region of the continental slope rather than at the coastline, and 2) there is a packing of streamlines in the area where the two boundary currents meet and head offshore. Strong gradients in this region are also evident in the thermal fields and in the sea surface

height. (This last field is actually the pressure at $z=0$, converted to an equivalent height via the hydrostatic relation.) Thus a counterpart of the separated Gulf Stream exists, even in the case of large diffusive parameters. It is clear from the overall smoothness of the patterns that there are no short-period transients. Although the 37 km grid size is small enough to resolve mesoscale eddies, their generation has been suppressed by the large subgrid-scale mixing.

The surface temperature is basically zonal in the mid-ocean, but shows strong effects of horizontal advection in the Gulf Stream region. Along the southeastern wall of the domain, the zonal pattern of isotherms is deformed by upwelling. The thermal structure at 500 m shows the existence of a large lens of warm water in the western part of the subtropical gyre.

5. The experiments following the spin-up

In the Laplacian experiment, values of $A_M=2\times 10^6$ $\text{cm}^2 \text{ s}^{-1}$ and $A_H=6\times 10^6$ $\text{cm}^2 \text{ s}^{-1}$ were specified for a continuing three-year integration with the 37 km grid size. The circulation very quickly evolved toward a more nonlinear state with weak mesoscale eddies. Although limitations on computer time did not allow an extended integration, experience with previous inte-

grations (e.g., Robinson *et al.*, 1977) showed that the major features of a statistical quasi-equilibrium state are reached after a few years. Thus an energy analysis was made at the end of the third year for a time period of 186 days.

The biharmonic experiment was initialized from the final state of the Laplacian experiment. Values of $B_M=0.8\times 10^{19}$ and $B_H=2.4\times 10^{19}$ $\text{cm}^4 \text{ s}^{-1}$ provided the same damping of two gridpoint features as the previous Laplacian coefficients, but reduced the lateral damping of mesoscale features by almost two orders of magnitude (cf. Section 3). Strong mesoscale disturbances developed and reached a state of statistical quasi-equilibrium during a $2\frac{1}{2}$ year integration. An energy analysis was made for a 400-day period at the end of the integration.

Fig. 5 shows the sea surface height at 8-day intervals in the Laplacian experiment. Along the path of the Gulf Stream jet, the flow is strong but quasi-steady. Transients are more evident in the region of nonlinear recirculation to the south of the Stream. Closed eddies develop there and move westward. The eddies have wavelengths of several hundred kilometers and periods of about 40 days. Farther away from the Gulf Stream, weaker fluctuations occur without actually forming

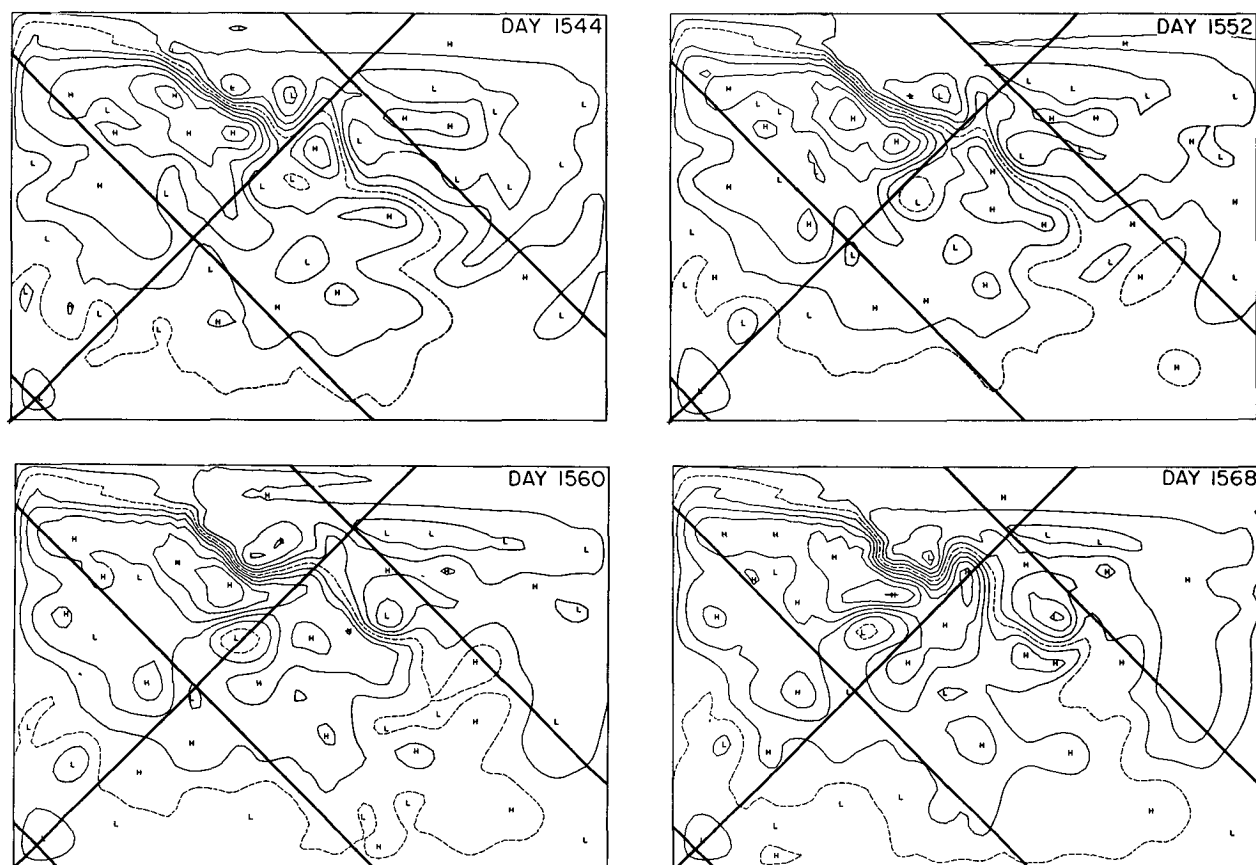


FIG. 8. Surface height fields in the biharmonic experiment (20 cm contour interval).

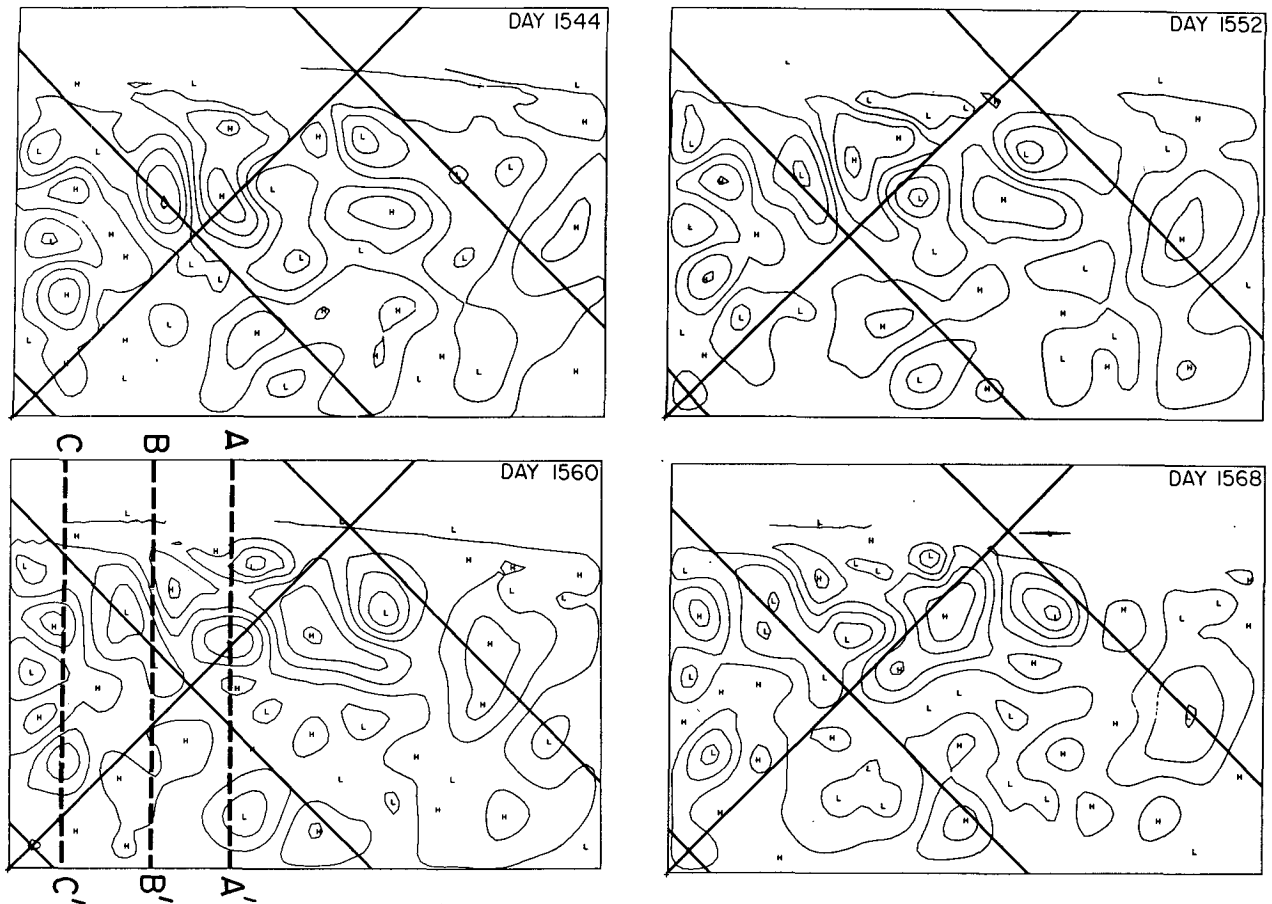


FIG. 9. Dynamic topography at 2700 db in the biharmonic experiment (10 cm contour interval).

many closed circulations at the surface. Their presence is more evident in the deep flow (Fig. 6). There, a secondary line of disturbances is seen to exist near 30°N . This is the region of the model's North Equatorial Current.

The fact that transients form mainly in westward-flowing currents immediately suggests that baroclinic instability may be the driving mechanism (cf. Gill *et al.*, 1974). The thermal structure of the eddies reveals only a weak baroclinic character, with temperature deviations from time-mean values rarely exceeding 0.25°C at thermocline depth (see Fig. 7). Nevertheless, the weak anomalies have been found to correlate well with vertical motion in some areas, indicating removal of potential energy from the time-averaged, large-scale thermal field.

The eddies in the Laplacian experiment are not as intense as those which are found in nature. It is now well known from observations that eddies can exhibit thermocline temperature anomalies of several degrees, particularly in the vicinity of the Gulf Stream, and that their presence can have a noticeable effect on the instantaneous path of the Stream. The Laplacian experiment, however, does give a reasonable simulation

of the time-averaged Gulf Stream; and it seems plausible that a realistic time-dependent Gulf Stream might be obtained if less damping were acting on the meso-scale disturbances.

Fig. 8 shows the sea surface height patterns about two years after changing to the scale-selective biharmonic closure scheme. There has been a large increase in eddy activity and in Gulf Stream meandering. (Note that the contour interval is now 20 cm instead of 10 cm). On day 1544, a blocking pattern, similar to what often occurs at the downstream ends of atmospheric jet streams, exists just east of the 72° meridian. An intense cyclonic disturbance forms within the trough of the blocking pattern and breaks off from the main stream. It then moves westward in the manner of a Gulf Stream ring.

The deep motion for the same sequence of days is shown in Fig. 9. (Here again, the contour interval is doubled over that in the Laplacian experiment.) The eddies are much stronger than in the other experiment (cf. Fig. 6). This is particularly clear when one realizes that the strongest deep currents in the Laplacian case were quasi-steady nonlinear recirculations near the Gulf Stream. In the biharmonic case, the eddies are so

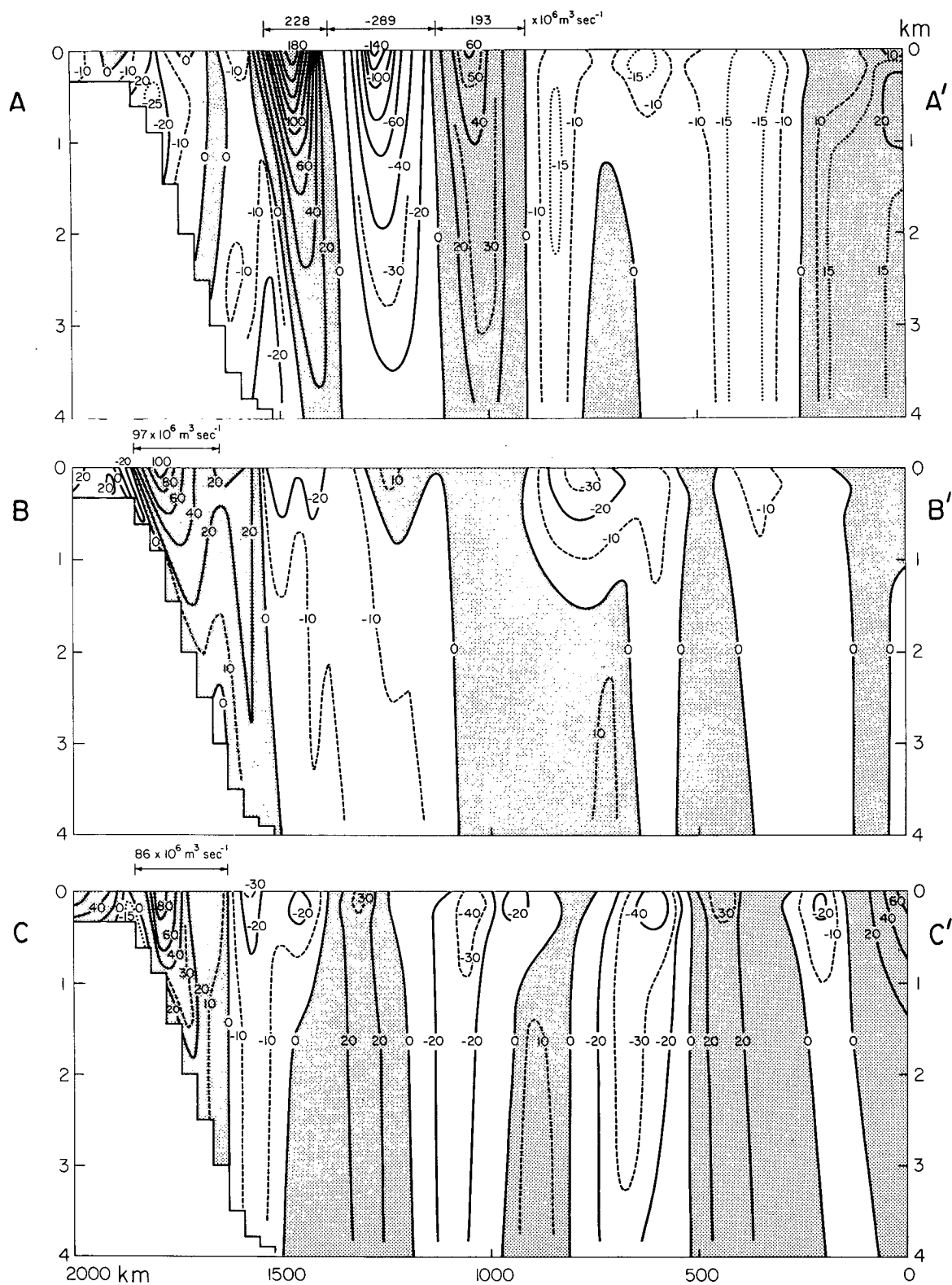


FIG. 10. Vertical sections of the normal velocity component (cm s^{-1}) on day 1560. The location of the sections is shown on Fig. 9.

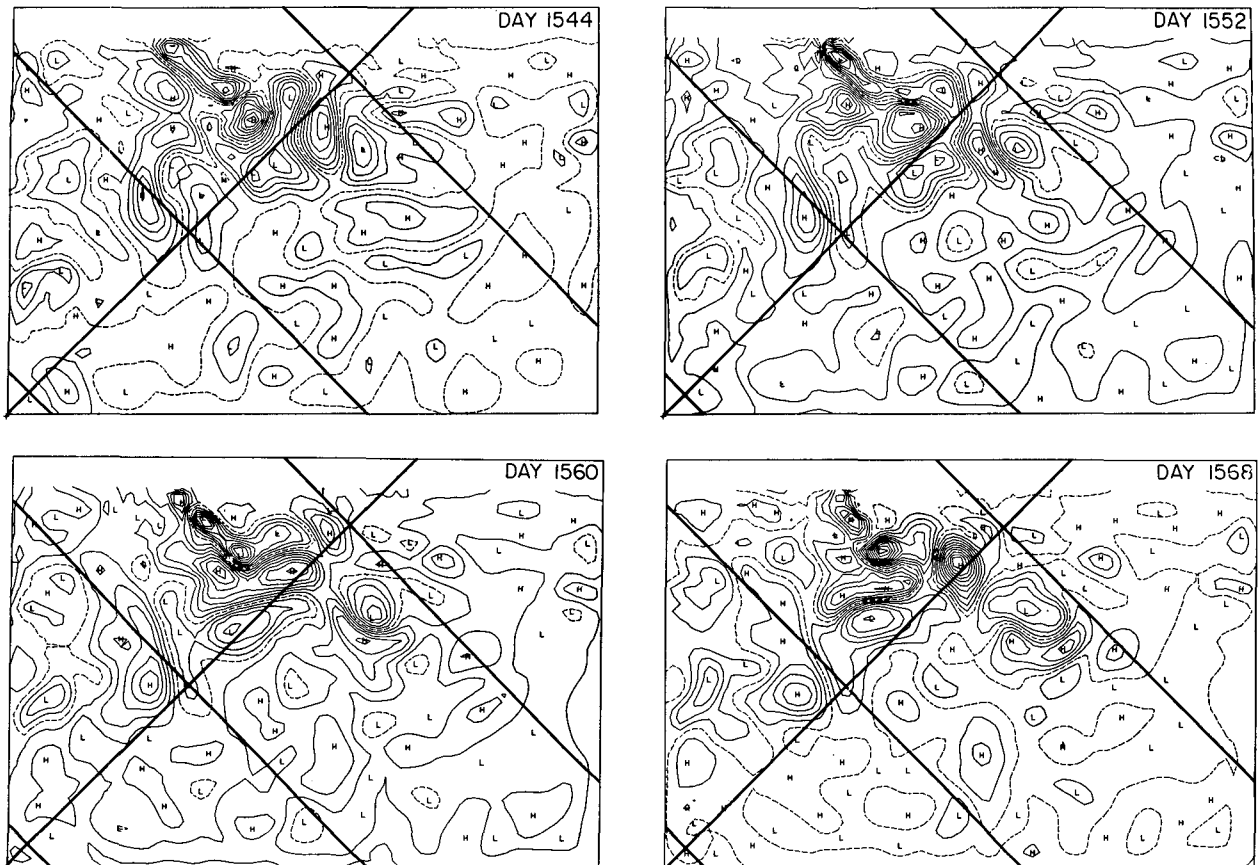


FIG. 11. Temperature deviation from time-mean values at 500 m for the biharmonic experiment (0.25°C contour interval).

intense that no mean pattern is evident. The eddy currents at 2700 m depth, in the vicinity of the Gulf Stream, are as large as $20\text{--}30\text{ cm s}^{-1}$.

Further insight into the flow patterns can be gained from Fig. 10, which shows three cross sections, normal to the coast, of the horizontal velocity component normal to the sections. From south of section C-C' until north of section B-B' the simulated Gulf Stream flows along the upper part of the continental slope as a narrow current with large vertical shear, and with maximum current speed of about 100 cm s^{-1} . Then the current turns abruptly eastward, increases in intensity, and, after reaching the abyssal plain, attains a maximum speed greater than 180 cm s^{-1} . Comparable velocities (and vertically integrated mass transports) are also found in the cutoff cyclonic ring: velocities of 140 cm s^{-1} toward the southwest and 60 cm s^{-1} toward the northeast at the surface; and velocities of 30 cm s^{-1} near the ocean bottom. Other eddies of lesser intensity are evident throughout the ocean interior.

Temperature deviations from time-mean values are shown in Fig. 11. The eddies clearly have a strong baroclinic structure. Near the Gulf Stream, the largest temperature difference between adjacent high and low

anomalies is 5°C ; and in the western portion of the North Equatorial Current, the largest difference is 2°C .

Surface temperature maps for the same sequence of days are shown in Fig. 12. The Gulf Stream appears as a meandering thermal front. Considerable temperature fluctuation also exists in the North Equatorial surface waters.

To show the variability associated with the eddies, Figs. 13 and 14 give the standard deviations of several variables in both experiments. The statistics are based on 186-day and 400-day periods, respectively, with a 2-day sampling interval. Both experiments exhibit maximum variability in the vicinity of the Gulf Stream, especially in the surface temperature, surface height and surface speed. In the Laplacian experiment, the streamfunction and surface pressure fields have double maxima associated with the regions of eastward flowing jet and westward flowing recirculation. Both experiments show a secondary zone of variability in a band between latitudes 25° and 30°N . The eddies in the biharmonic case are about twice as strong as in the Laplacian case.

To conclude this section, we show the patterns that result after the eddies are removed by time averaging

(Figs. 15 and 16). These fields may be compared with the quasi-steady results of the highly viscous spin-up calculation (Fig. 4). It should be noted that the contour interval for ψ and p , is twice as large in Fig. 16 as in Figs. 4 and 15.

It is evident that by reducing the coefficients for Laplacian diffusion of heat and momentum, a more nonlinear flow pattern develops in the vicinity of the Gulf Stream. Two recirculating gyres form in the deep ocean adjacent to the continental slope, with transport maxima of 180 Sv in the anticyclonic gyre and 135 Sv in the cyclonic one. Temperature gradients sharpen in the vicinity of the Gulf Stream jet, and horizontal advection of warm water by the Stream is enhanced.

When the effects of diffusion are kept the same for the smallest resolvable length scales but reduced for the larger scales (the biharmonic experiment), a seemingly paradoxical result occurs. The time-averaged fields become more like what they were in the highly diffusive Laplacian spin-up experiment. This indicates that when the growth of mesoscale eddies is not inhibited by excessive friction acting at their length scale, then the eddies achieve finite-amplitude proportions and act to remove the energy contained in the mean field. Thus, judging from their visible effects on

the time-averaged fields, the eddies act as explicit diffusers of heat and momentum.

Two aspects of the time-mean flow appear more realistic in the biharmonic case than in the Laplacian case. The first is that the intensity of the northern cyclonic gyre, relative to that of the subtropical anticyclonic gyre, drops considerably. The second aspect is that the strong surface recirculation south of the Gulf Stream does not appear in the biharmonic experiment. This pattern of a broad westward-flowing return current, south of the intense eastward-flowing Gulf Stream, is in better agreement with the observed surface drift pattern.

In both experiments, the separation point of the mean Gulf Stream is somewhat to the south of the latitude of zero wind stress curl (37°N), especially in the biharmonic case. This is different from Han's (1975) flat-bottom ocean simulation, in which a large overshoot to the north occurred (cf. Fig. 3). It appears that bottom topography, and possibly also the orientation of the coastline, are important in determining the separation point. Similar conclusions for a barotropic ocean, with and without bottom topography, were obtained by Lee (1976); but further experiments involv-

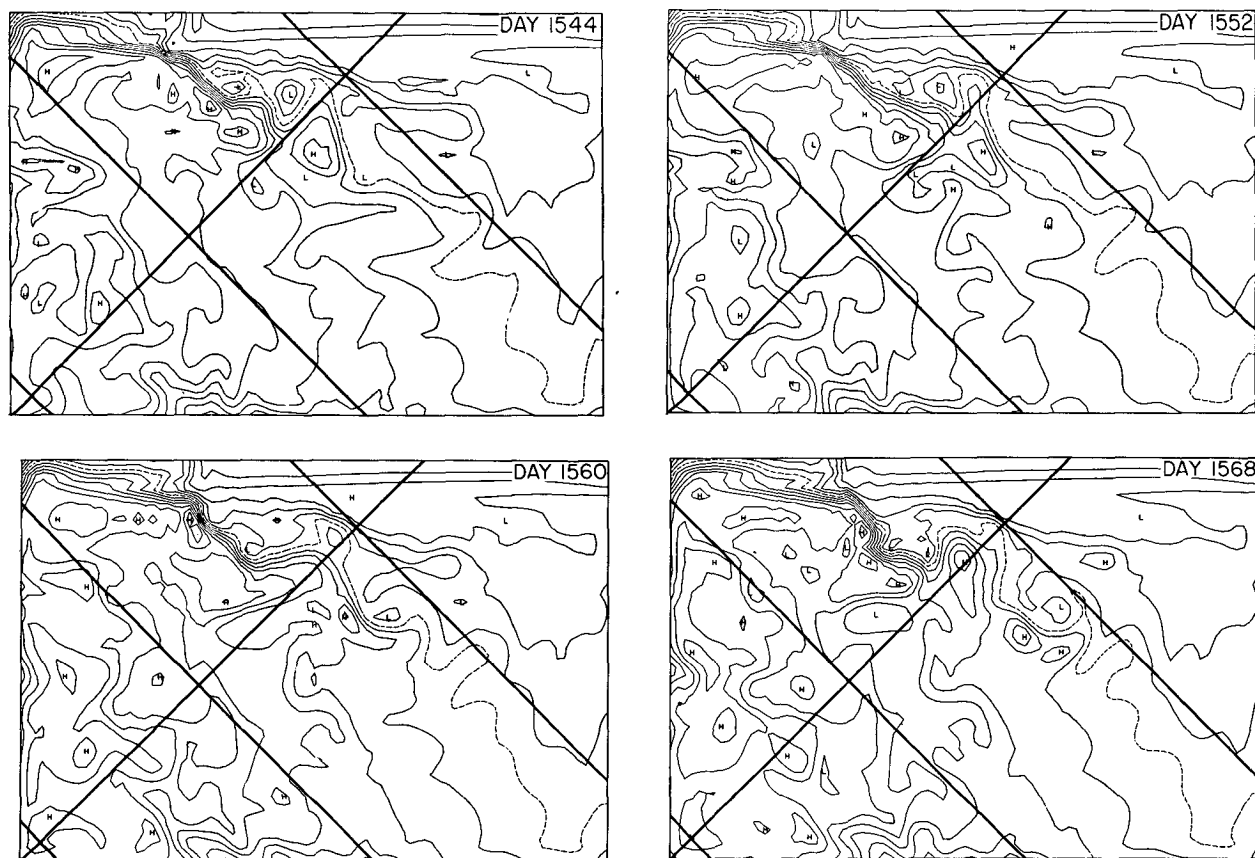


FIG. 12. Sea surface temperature in the biharmonic experiment. Contour interval is 1°C .

ing topography using baroclinic models may be needed to understand the separation mechanism in detail.

6. Energy analysis

In order to understand the dynamics of the eddies and their interaction with the time-mean circulation, we have investigated the energy transfers in the two eddy experiments. It is convenient to introduce the following notation:

- time average
- ' time deviation
- ~ horizontal space average
- * horizontal space deviation
- () volume average

$\frac{1}{S} \int \cdot dS$ horizontal average at the ocean surface or bottom.

Using this notation, mean kinetic energy \bar{K} and eddy kinetic energy K' are defined by

$$\bar{K} = \left\langle \frac{\bar{u}^2 + \bar{v}^2}{2} \right\rangle, \quad (14)$$

Mean available potential energy and eddy available potential energy are defined as in Han (1975):

$$\bar{P} = \alpha g \left\langle \frac{1}{2} (\bar{T}')^2 \left(\frac{\partial \bar{T}}{\partial z} \right)^{-1} \right\rangle, \quad (16)$$

$$P' = \alpha g \left\langle \frac{1}{2} (\bar{T}')^2 \left(\frac{\partial \bar{T}}{\partial z} \right)^{-1} \right\rangle. \quad (17)$$

By standard manipulations of the governing equations, one can show that the time-rates-of-change of the various energies are

$$\begin{aligned} \frac{\partial \bar{K}}{\partial t} = & -\{\bar{K}:K'\} - \{\bar{K}:\bar{P}\} + \{\tau^w:\bar{K}\} - \{\bar{K}:\tau^b\} \\ & - \{\bar{K}:\kappa\} - \{\bar{K}:A_M\}, \end{aligned} \quad (18)$$

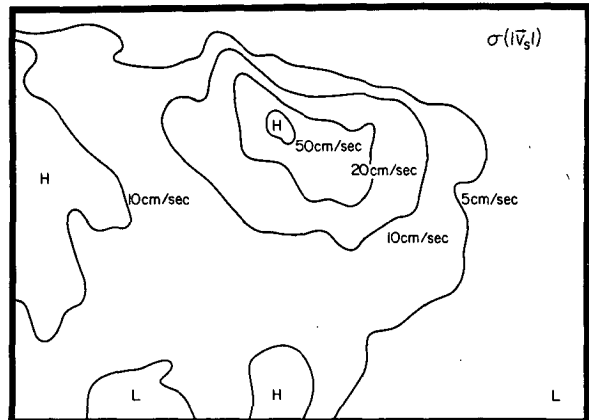
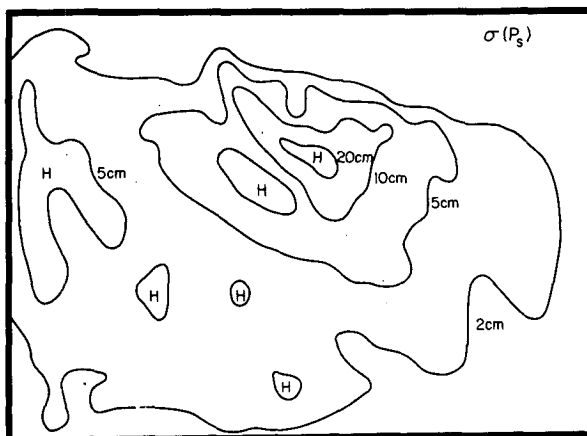
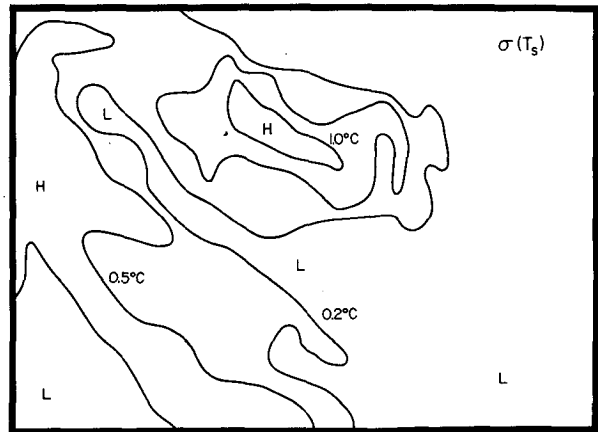
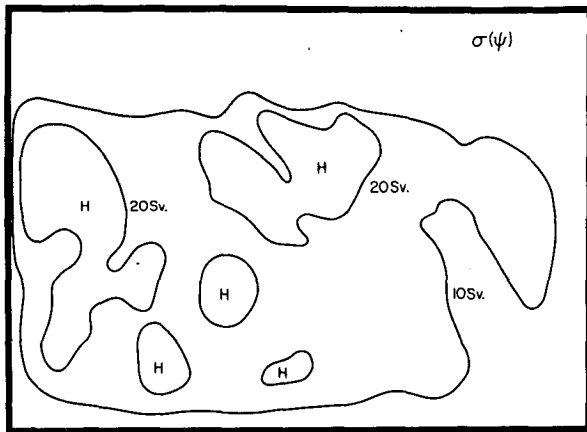


FIG. 13. The standard deviation of fields in the Laplacian experiment.

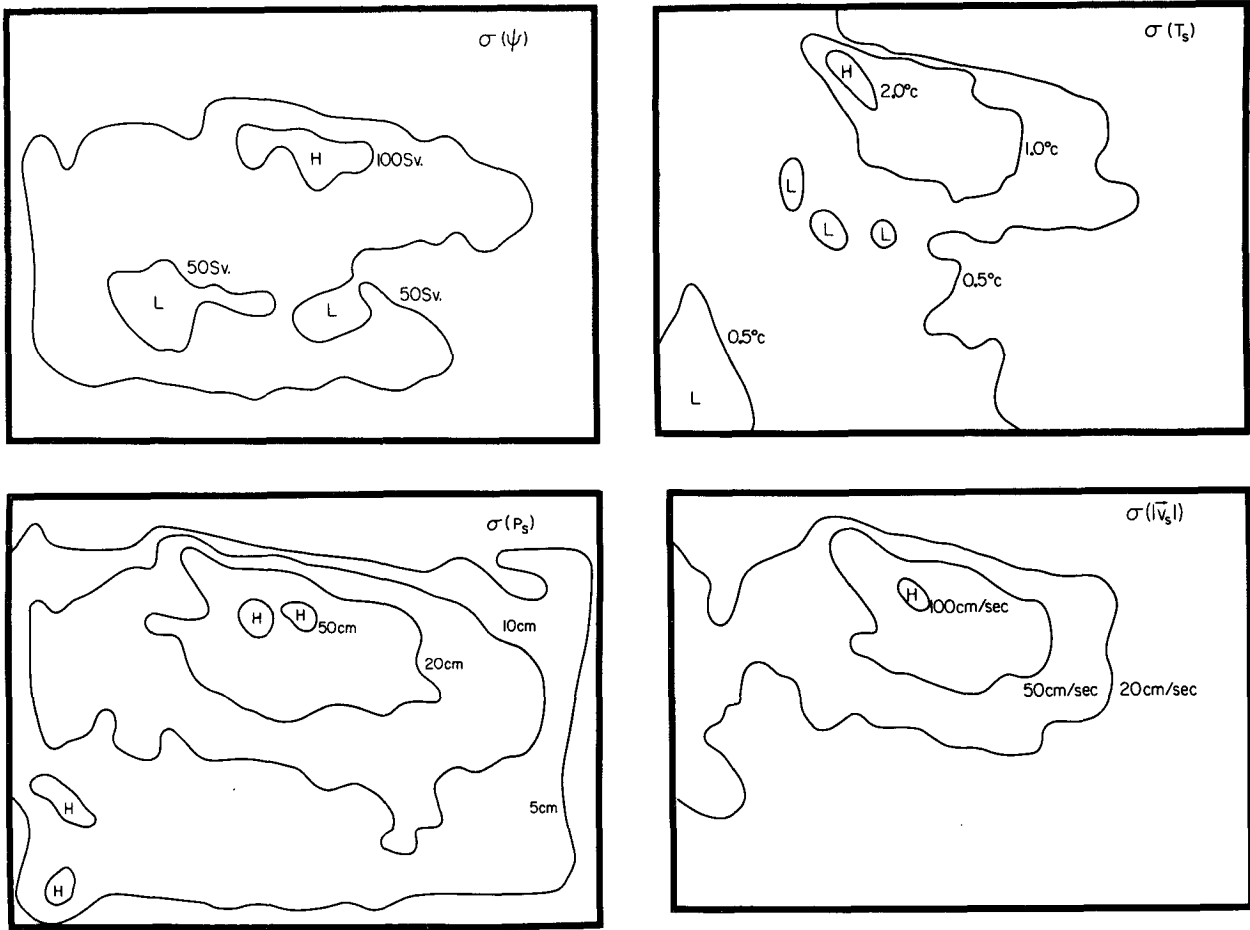


FIG. 14. The standard deviation of fields in the biharmonic experiment.

$$\frac{\partial K'}{\partial t} = \{\bar{K}:K'\} + \{P':K'\} - \{K':\tau^b\} - \{K':\kappa\} - \{K':A_M\}, \quad (19)$$

$$\frac{\partial \bar{P}}{\partial t} = \{\bar{K}:\bar{P}\} - \{\bar{P}:P'\} + \{T^A:\bar{P}\} - \left\{\bar{P}:\frac{\kappa}{\delta}\right\} - \{\bar{P}:A_H\}, \quad (20)$$

$$\frac{\partial P'}{\partial t} = -\{P':K'\} + \{\bar{P}:P'\} + \{T^A:P'\} - \left\{P':\frac{\kappa}{\delta}\right\} - \{P':A_H\}. \quad (21)$$

In the above, exchanges between two energy types are given by

$$\{\bar{K}:K'\} = \left\langle \bar{v} \cdot \left(\nabla \cdot \bar{v}' + \frac{\partial \bar{w}'v'}{\partial z} \right) \right\rangle, \quad (22)$$

$$\{\bar{P}:P'\} = g\alpha \left\langle \bar{T}^* \nabla \cdot \bar{v}' T'^* \left(\frac{\partial \bar{T}'}{\partial z} \right)^{-1} \right\rangle, \quad (23)$$

$$\{\bar{K}:\bar{P}\} = -g\alpha \langle \bar{T}' \bar{w} \rangle, \quad (24)$$

$$\{P':K'\} = g\alpha \langle \bar{T}' \bar{w}' \rangle. \quad (25)$$

The effects of wind driving and bottom friction on kinetic energy are

$$\{\tau^w:\bar{K}\} = \frac{1}{S} \int \bar{v}|_{z=0} \cdot \tau^w dS, \quad (26)$$

$$\{\bar{K}:\tau^b\} = \frac{1}{S} \int \bar{v}|_{z=-H} \cdot \tau^b dS, \quad (27)$$

$$\{K':\tau^b\} = \frac{1}{S} \int \bar{v}'|_{z=-H} \cdot \tau^b dS. \quad (28)$$

The effects of thermal forcing at the ocean surface are

$$\{T^A:\bar{P}\} = \frac{g\alpha\gamma}{S} \int \bar{T}^* \langle T^A - \bar{T}^* \rangle \left(\frac{\partial \bar{T}'}{\partial z} \right)^{-1} dS, \quad (29)$$

$$\{T^A:P'\} = \frac{g\alpha\gamma}{S} \int -\langle T'^* \rangle^2 \left(\frac{\partial \bar{T}'}{\partial z} \right)^{-1} dS. \quad (30)$$

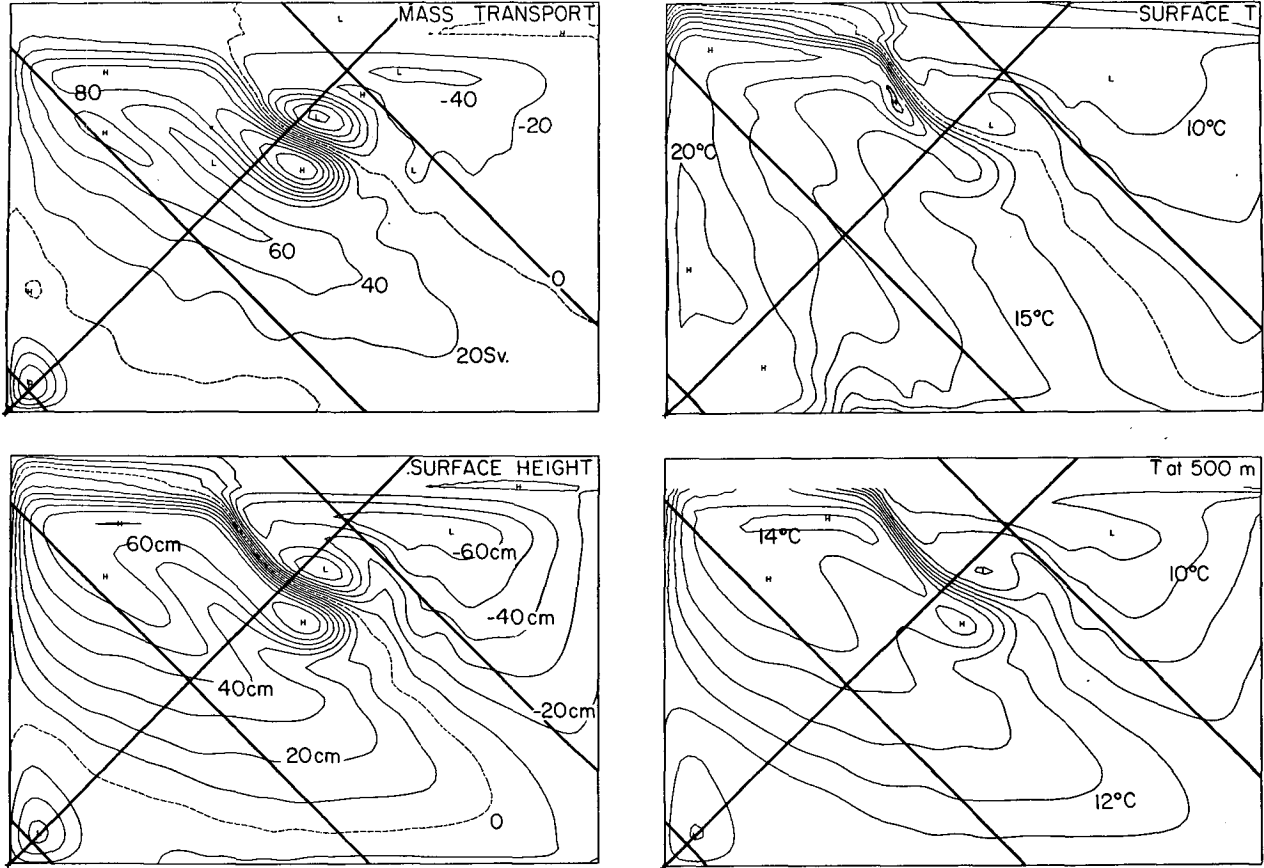


FIG. 15. Time-averaged fields in the Laplacian experiment.

Dissipations of energy due to *internal* vertical diffusion (including convective overturning) are

$$\left\{ \bar{P} : \frac{\kappa}{\delta} \right\} = -g\alpha \left\langle \bar{T}^* \frac{\partial^2 \bar{T}^*}{\partial z^2} \left(\frac{\partial \bar{T}}{\partial z} \right)^{-1} \right\rangle + \{ T^A : \bar{P} \}, \quad (31)$$

$$\left\{ P' : \frac{\kappa}{\delta} \right\} = -g\alpha \left\langle \overline{T'^* \frac{\partial^2 T'^*}{\partial z^2}} \left(\frac{\partial \bar{T}}{\partial z} \right)^{-1} \right\rangle + \{ T^A : P' \}, \quad (32)$$

$$\{ \bar{K} : \kappa \} = \left\langle \frac{\partial \bar{v}}{\partial z} \cdot \frac{\partial \bar{v}}{\partial z} \right\rangle, \quad (33)$$

$$\{ K' : \kappa \} = \left\langle \frac{\partial v'}{\partial z} \cdot \frac{\partial v'}{\partial z} \right\rangle. \quad (34)$$

Losses of energy due to lateral mixing of momentum and lateral diffusion of heat are given by

$$\{ \bar{K} : A_M \} = -\langle \bar{v} \cdot A_M \nabla^2 \bar{v} \rangle, \quad (35)$$

$$\{ K' : A_M \} = -\langle v' \cdot A_M \nabla^2 v' \rangle, \quad (36)$$

$$\{ \bar{P} : A_H \} = -g\alpha \left\langle \bar{T}^* A_H \nabla^2 \bar{T}^* \left(\frac{\partial \bar{T}}{\partial z} \right)^{-1} \right\rangle, \quad (37)$$

$$\{ P' : A_H \} = -g\alpha \left\langle \overline{T'^* A_H \nabla^2 T'^*} \left(\frac{\partial \bar{T}}{\partial z} \right)^{-1} \right\rangle, \quad (38)$$

with appropriate modifications for the biharmonic closure scheme. For purpose of illustration, all of these energy transfers can be combined in a box diagram, as shown in Fig. 18 (top left).

As indicated in the previous section, time periods of 186 days and 400 days were selected for analysis of the Laplacian experiment and biharmonic experiment, respectively. The time records of eddy potential and kinetic energies for these periods are shown in Fig. 17. The records seem to be composed of a variety of time scales ranging from 15 to 150 days, with no really dominant period. The total time sampled in the Laplacian case may be too short to give completely reliable statistics, but the record for the biharmonic experiment appears to be long enough and also devoid of secular trend. In both experiments, there is an approximate equipartition of eddy energy into kinetic and potential forms, but the energy levels are much higher in the biharmonic case.

Basin-averaged energy transfers for the two experiments are shown in Fig. 18. Also shown for comparison is a similar diagram from the numerical study of Han

(1975), in which diffusion coefficients $A_M = 2 \times 10^6$ and $A_H = 5 \times 10^6 \text{ cm}^2 \text{ s}^{-1}$ were used. Except for the effect of vertical diffusion and convection on available potential energy, all of these transfers were computed using finite-difference forms of the energy equations which are consistent with the finite-difference prognostic equations. (In the topographic experiments, vertical diffusive effects were evaluated as residuals, and therefore also include any time-rates-of-change of \bar{P} or P' .) Although these block diagrams cannot indicate the regional distribution of the various energy transfer processes, they nevertheless give considerable insight into the overall physics of the eddies and the mean circulation.

As far as external forcing is concerned, the major input of energy in each of the experiments comes from the wind stress. Net work by wind is smaller in the study of Han (1975) than in the present two cases, not only because the wind stress amplitude is smaller (2 dyn cm^{-2}) but also because the strong currents there are mainly orthogonal to the wind (see Fig. 3). In each of the three experiments, the thermal forcing provides a significant (but not dominant) input of energy into the mean available potential energy.

Some of the wind-produced energy of the mean currents is immediately lost by friction. In the two

topographic cases, the loss by bottom friction is larger than the loss by lateral friction because the strong boundary currents are in relatively shallow water. (The effect of internal vertical friction, on the other hand, is so small that it is not even included in the diagrams.) The lateral frictional losses of \bar{K} are smaller by more than a factor of 2 with the biharmonic closure scheme.

In all of the cases, the mean currents mainly act to create mean available potential energy (e.g., by creating the subtropical lens of warm water through Ekman transport and Ekman pumping), rather than to create eddy kinetic energy by direct barotropic breakdown of the flow. In the two experiments with Laplacian closure, lateral diffusion of heat removes so much available potential energy from the time-averaged fields that little is left for transfer to eddy available potential energy. But with the biharmonic closure condition, diffusive losses are reduced and the baroclinic instability process ($\bar{P} \rightarrow P' \rightarrow K'$) is greatly enhanced.

Significant baroclinic instability would probably occur without using biharmonic heat diffusion, if the Laplacian coefficient A_H were reduced sufficiently. However, a costly increase in grid resolution would be required in order to suppress computational noise.

The diffusive loss of P' is very large in the biharmonic case, but that is because P' is so large. Over a period of

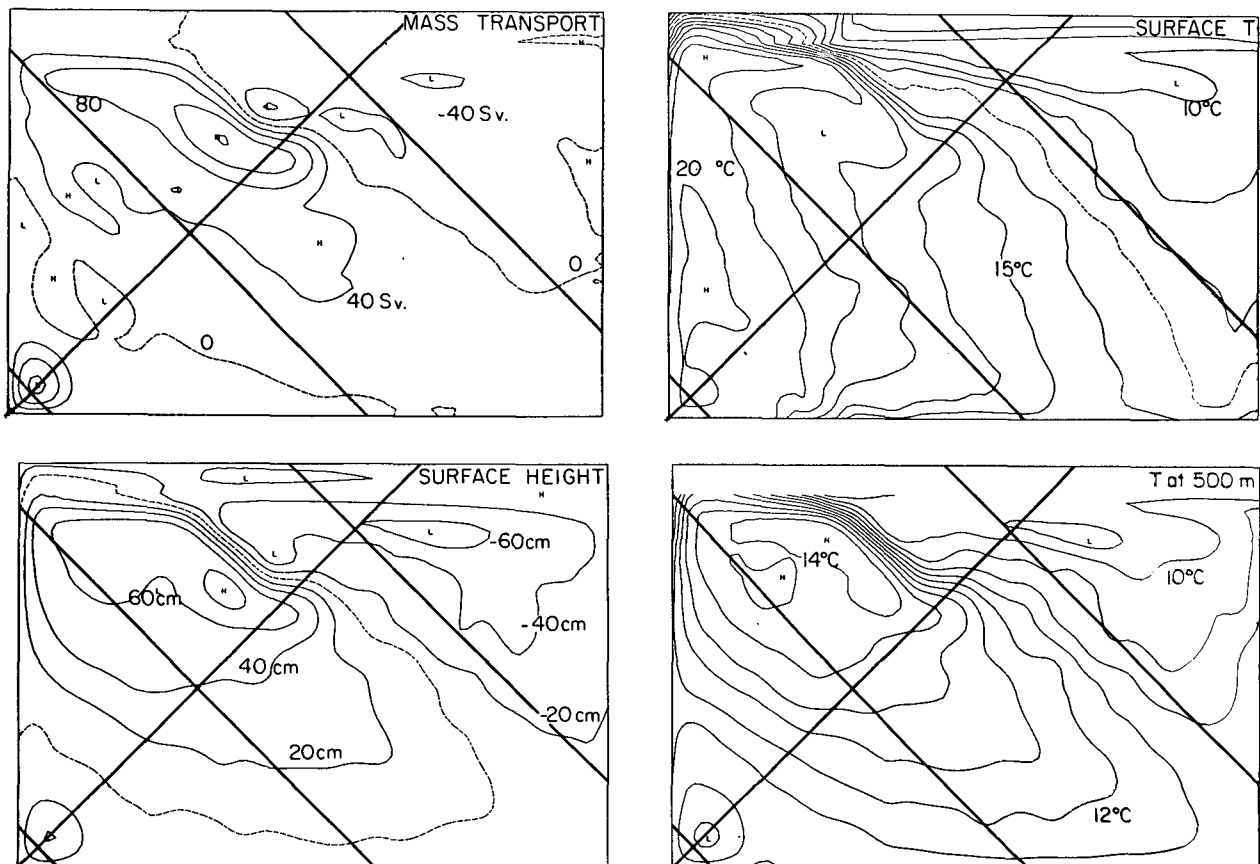


FIG. 16. Time-averaged fields in the biharmonic experiment.

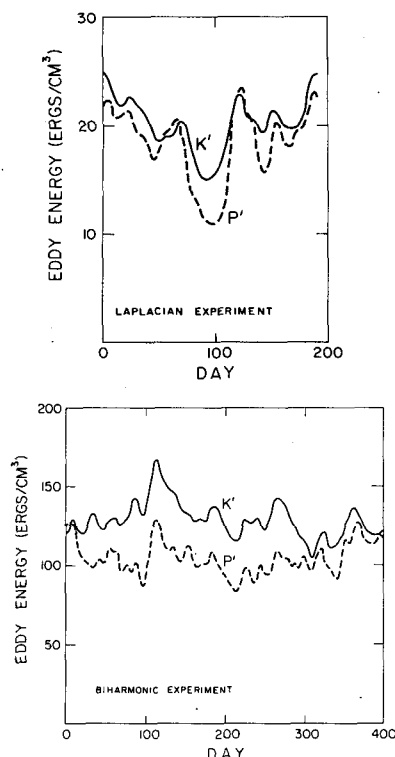


FIG. 17. Eddy kinetic energy and eddy potential energy over the time intervals chosen for analysis.

10 days, about 20% of the total P' would be lost to biharmonic diffusion, whereas more than 50% would be lost to Laplacian diffusion in the same time.

Finally, we note that in the biharmonic experiment bottom friction is more important than lateral friction in dissipating eddy kinetic energy. A further reduction in the value of B_M may have little qualitative effect on the simulated currents, and the present results may be indicative of what happens when bottom friction is the dominant mechanism for kinetic energy dissipation.

Further insight into the energetics can be gained by looking at the horizontal variations in the energy transfer rates after making only a vertical integration. Fig. 19 shows three energy conversion terms (on the left) and three dissipation terms (on the right), which affect the eddy energy in the biharmonic experiment. It should be noted that the conversion terms have regions of positive and of negative values, and that the contour lines are logarithmically spaced by a factor of two (except in the $\{\bar{P}:P'\}$ conversion, where a factor of 4 is used). The transfer terms for the Laplacian experiment will not be shown, since they are fairly similar.

The barotropic generation term $\{\bar{K}:K'\}$ and the baroclinic generation term $\{P':K'\}$ both show concentrated production of eddy kinetic energy in that part of the Gulf Stream which lies over the continental slope. Thus, a mixed baroclinic-barotropic instability

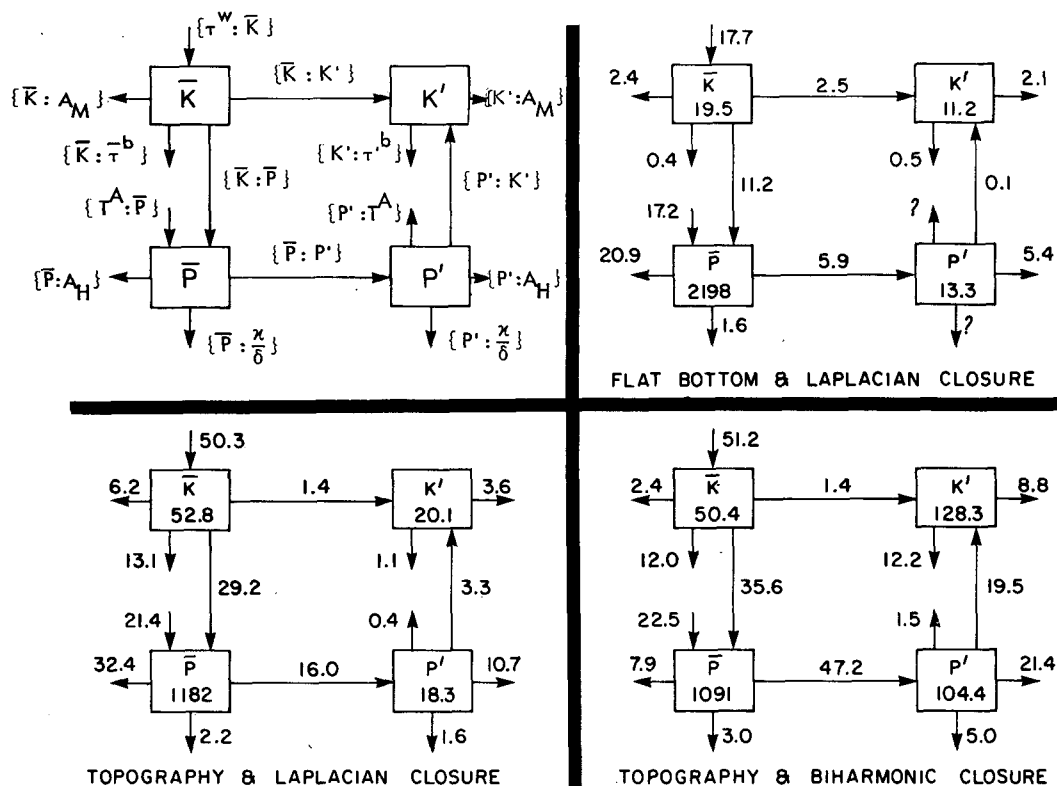


FIG. 18. Basin-averaged energy diagrams. Energies are in ergs cm^{-3} and transfer rates are in $10^{-6} \text{ ergs cm}^{-3} \text{ s}^{-1}$. Top left: schematic; top right: energetics for the experiment of Han (1975); lower left: energetics for the Laplacian experiment; lower right: energetics for the biharmonic experiment.

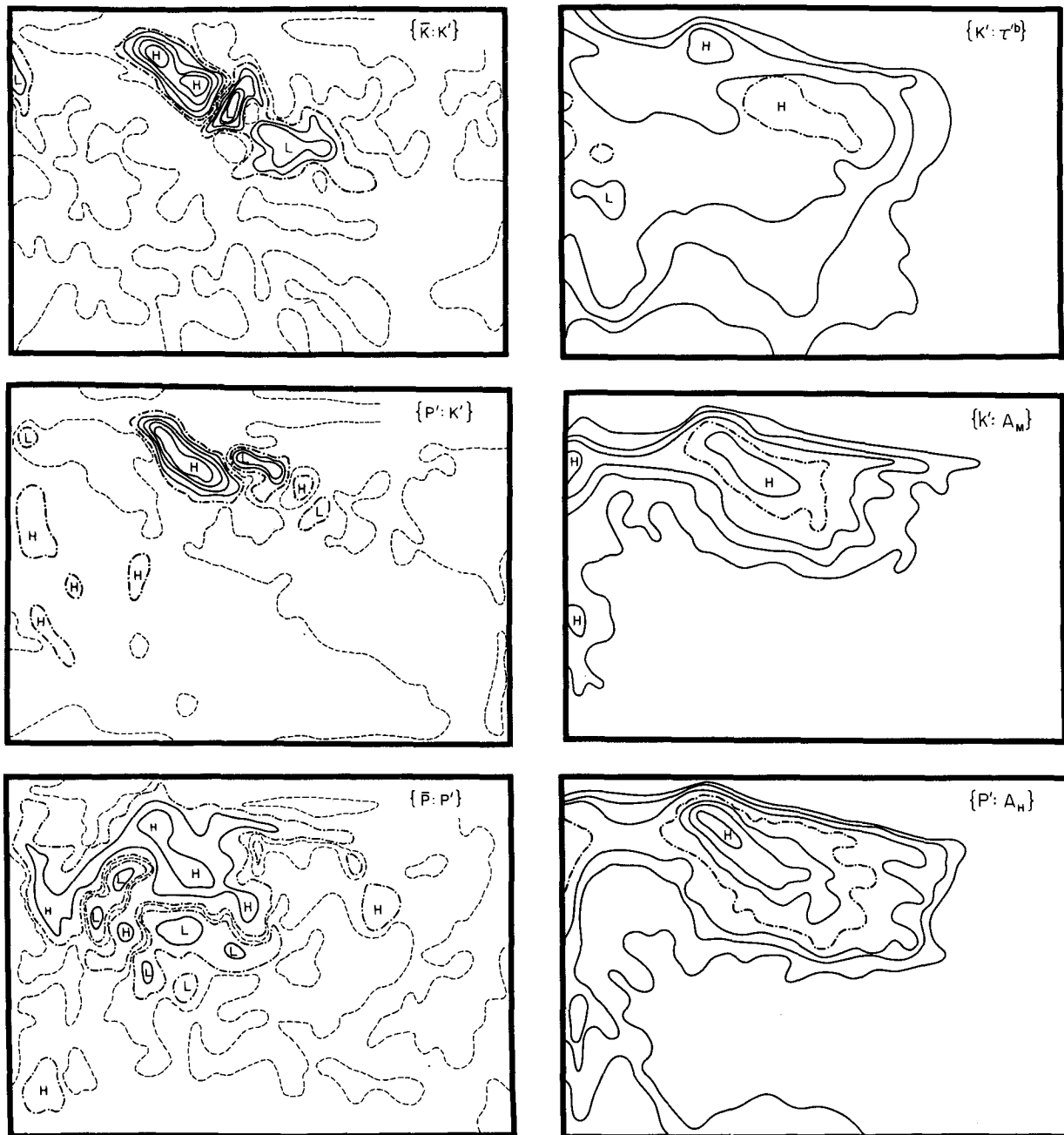


FIG. 19. The horizontal distribution of transfers affecting eddy energy in the biharmonic experiment. The dot-dash lines represent the same conversion rate for all processes. For the production processes on the left: (i) the zero line is dashed; (ii) positive and negative regions are distinguished by H and L symbols; and (iii) each solid line represents an increase in the magnitude of the transfer rate by a factor of 2 (or 4, in the $\{\bar{P}:P'\}$ transfer). For the dissipation processes on the right: (i) each solid line within the closed dot-dash lines represents a two-fold increase in dissipation rate, and (ii) each of the three solid lines outside the closed dot-dash lines represents a two-fold decrease in dissipation rate.

exists there. Farther downstream there is a transfer from K' back to \bar{K} , in the manner of a negative viscosity effect. Thus, the mean Gulf Stream in the deep ocean is at least partially maintained by the eddies. The positive and negative portions of $\{\bar{K}:K'\}$ almost cancel out, so that the barotropic instability process is weak when considering the ocean as a whole. Away from the Gulf Stream, there are regions of baroclinic

instability in the North Equatorial Current, but the conversion rate $\{P':K'\}$ is fairly small.

The potential energy transfer term $\{\bar{P}:P'\}$ indicates generation of eddy potential energy in approximately the same regions where the term $\{P':K'\}$ is positive, as would be expected for baroclinic instability. There are also regions where potential energy goes from eddies to the mean state. One of these is an area where the

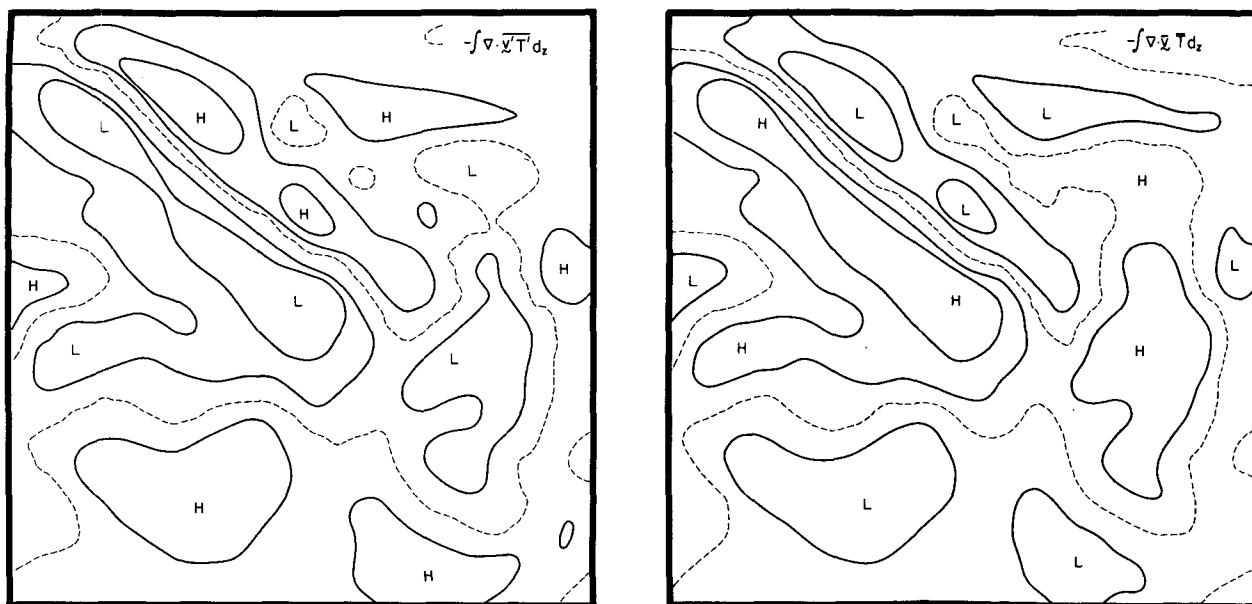


FIG. 20. Heat transport due to mean currents (right) and due to eddies (left) for a $1000 \text{ km} \times 1000 \text{ km}$ region centered on the Gulf Stream jet. (The zero line is dashed.)

simulated Gulf Stream rings are reabsorbed into the Stream. This may indicate that the rings impart potential energy to the mean state as they weaken, in a manner similar to that of occluding atmospheric cyclones.

The dissipation of eddy kinetic energy by lateral friction $\{K':A_M\}$ is concentrated along the path of the mean Gulf Stream, especially in that portion above the continental slope. Most of the dissipation is far enough into the interior not to be sensitive to the lateral boundary conditions. The removal of eddy energy by bottom friction $\{K':\tau'^b\}$ occurs over a much larger area, and much of the energy loss takes place in the mid-ocean portion of the subtropical gyre.

7. Heat transport

Two decades of simulated time are not long enough to achieve thermal equilibrium in the two lowest layers of the model ocean, and hence not long enough to achieve an equilibrium heat transport by overturning in the meridional plane. Nevertheless, tentative conclusions about other aspects of the heat transport are possible.

It was suggested in Section 5 that eddies act as explicit horizontal diffusers of heat, judging from the appearance of the time-averaged surface temperature. Fig. 20 gives a quantitative verification of this. The net heat transport by eddies almost exactly offsets the transport by the mean currents in a $1000 \text{ km} \times 1000 \text{ km}$ region centered on the Gulf Stream. This means that both the time-rate-of-change of the mean thermal field and the effect of the subgrid-scale diffusion are small. It is possible to compute the effective eddy diffusivity

due to the resolved eddies themselves, i.e.,

$$A_E = - \int \nabla \cdot (\overline{\mathbf{u}'T'}) dz / \int \nabla^2 \overline{T} dz.$$

In the vicinity of the Gulf Stream, the value of A_E is typically in the range $1\text{--}3 \times 10^7 \text{ cm}^2 \text{ s}^{-1}$.

The effect of the eddies on the vertical transport of heat has also been examined. Heating rates due to vertical eddy motion have been found to be small, compared with the heating (or cooling) due to vertical advection by the mean flow. Typically, the mean vertical advection term $\partial(\overline{wT})/\partial z$ is at least an order of magnitude larger than the eddy term $\partial(\overline{w'T'})/\partial z$. It is possible, however, that eddies might transfer more heat if the subgrid-scale diffusive effects were reduced by using smaller values of κ and B_H .

8. Conclusions

The present experiments show that fairly realistic simulations of the ocean circulation can be made with a primitive equation model. Part of the satisfactory model performance is due to the small grid size, but the integral constraints maintained by the differencing scheme and the highly scale-selective closure hypothesis are also important.

The numerical simulations show that a meandering Gulf Stream jet and mid-ocean mesoscale eddies of a realistic kind will form spontaneously in the model ocean, provided that the lateral diffusive effects are sufficiently small. A combined baroclinic-barotropic instability occurs in the Gulf Stream region above the continental slope, but the eddies transfer some kinetic

energy back to the mean flow after the Gulf Stream reaches the abyssal plains. A weak baroclinic instability is found in the North Equatorial Current. Most of the dissipation of the eddy kinetic energy, as well as the energy of the time-mean currents, is by bottom friction. The eddies are an explicit mechanism for heat transport, whose effect in the Gulf Stream region is comparable to a lateral diffusion coefficient of $10^7 \text{ cm}^2 \text{ s}^{-1}$; and thus eddies can have a significant long-term influence on the thermal structure of the ocean.

We have characterized the statistical states, reached after a few years of integration in each of the fine grid experiments, as "quasi-equilibrium" states. By this we mean that the eddy energy curves (cf. Fig. 17) do not show much secular trend over the record length. This is especially true in the biharmonic experiment. Furthermore, the time rate of change of mean available potential energy (when combined with vertical diffusive effects in the $\{\bar{P}:\kappa/\delta\}$ term of Fig. 18) seems small, relative to the other terms. We cannot rule out the possibility that significant changes in the overall thermal field might ultimately occur over periods of decades. However, we are encouraged by the fact that eddies are highly diffusive (except for the effect on time-mean current structure for a portion of the Gulf Stream above the abyssal plain) to think that the results will not change much from that of the coarse-grid longer term simulation, as far as time-mean fields are concerned. In any event, the computer resources that would be required for a long-term integration in the fine grid are prohibitive at this time. A similar remark applies for investigating the effects of reduced grid size and reduced horizontal diffusion parameters. At the very least, the eddy amplitudes and eddy energetics are in quasi-equilibrium with the existing thermal structure; and since this structure looks realistic, the conclusions about eddies and their energetics should be basically correct.

Many of the results that are obtained with this wind and thermally driven primitive-equation model are similar to those that are obtained by Holland (1977) with an adiabatic quasi-geostrophic two-layer model. He also finds that mesoscale eddies originate mainly from baroclinic-barotropic instabilities of the Gulf Stream, and that their energy is ultimately removed by bottom friction over a broad area of the mid-ocean. Holland finds that the eddy energy in the deep water is maintained primarily by the downward transfer of eddy kinetic energy through the term $\overline{w'p'}$. We have calculated the downward energy transfer to the lowest model layer by the pressure work term $\overline{w'p'}$ and find that in the biharmonic experiment it amounts to 62% of the eddy energy dissipation by bottom friction. Thus, the deep eddies are driven mainly by the pressure work term, both in the primitive-equation and the quasi-geostrophic models.

One point of difference between the simulations with

the two models is that the eddies drive the time-averaged deep flow in Holland's adiabatic model; whereas the eddies may be retarding the time-averaged deep flow in the primitive equation model, because in the biharmonic experiment, which has vigorous eddies, the time-averaged deep currents below the Gulf Stream are only about half as strong as in the Laplacian experiment, which has much weaker eddies. This suggests that thermal forcing plays an important role in maintaining the time-averaged deep flow.

Acknowledgments. The authors wish to thank W. R. Holland for suggesting the biharmonic closure formulation, Y.-J. Han for helpful remarks on analyzing basin energetics, and other colleagues in POLYMODE for valuable comments. They also thank D. K. Conti for developing the computer plotting program, B. Gladstone for drafting some of the figures, and K. Nolan and S. Lovell for typing the manuscript.

The work was supported by the National Science Foundation, Office of Climate Dynamics (Grant OCD 72-01502) and Office for the International Decade of Ocean Exploration (Grant IDO 74-22505), and by the National Aeronautics and Space Administration, Wallops Flight Center (Contract NAS 6-2703).

REFERENCES

- Anderson, D. W., F. J. Sparacio and R. M. Tomasulo, 1967: Machine philosophy and instruction handling. *IBM J. Res. Dev.*, **11**, 8-24.
- Arakawa, A., 1966: Computational design for long-term numerical integration of the equations of fluid motion: Two-dimensional incompressible flow. Part I. *J. Comput. Phys.*, **1**, 119-143.
- , 1972: Design of the UCLA general circulation model. Numerical Simulation of Weather and Climate, Tech. Rep. No. 7, Dept. Meteor., UCLA, 116 pp.
- Blandford, R. R., 1971: Boundary conditions in homogeneous ocean models. *Deep-Sea Res.*, **18**, 739-751.
- Bryan, K., 1969: A numerical method for the study of the circulation of the world ocean. *J. Comput. Phys.*, **4**, 347-376.
- Chen, J.-H., 1971: Finite difference methods and the leading edge problem. Ph.D. thesis, Princeton University, 102 pp.
- Gill, A. E., J. S. A. Green and A. J. Simmons, 1974: Energy partition in the large-scale ocean circulation and the production of mid-ocean eddies. *Deep-Sea Res.*, **21**, 499-528.
- Haidvogel, D. B., 1976: The sensitivity and predictability of mesoscale eddies in an idealized ocean model. Ph.D. thesis, MIT, 250 pp.
- Han, Y.-J., 1975: Numerical simulation of mesoscale ocean eddies. Ph.D. thesis, UCLA, 154 pp.
- Haney, R. L., 1974: A numerical study of the response of an idealized ocean to large-scale surface heat and momentum flux. *J. Phys. Oceanogr.*, **4**, 145-167.
- Holland, W. R., 1977: Numerical experiments on the role of mesoscale eddies in the general circulation of the ocean. In preparation.
- , and L. B. Lin, 1975: On the generation of mesoscale eddies and their contribution to the oceanic general circulation. Parts I and II. *J. Phys. Oceanogr.*, **5**, 642-669.
- Huppert, H. E., and K. Bryan, 1976: Topographically generated eddies. *Deep-Sea Res.*, **23**, 655-679.
- Joint POLYMODE Working Groups, 1976: Variability of ocean currents and the general ocean circulation: Review and

- current status of the problem. Report of the February 1976 Joint POLYMODE Executive Committee Meeting, Appendix II.
- Koshlyakov, M. N., and Y. M. Grachev, 1973: Mesoscale currents at a hydrophysical polygon in the tropical Atlantic. *Deep-Sea Res.*, **20**, 507-526.
- Lee, T.-N., 1976: Numerical calculations of the wind-driven circulation in a barotropic ocean. Ph.D. thesis, UCLA, 191 pp.
- MODE-I Dynamics Group, 1975: Dynamics and the analysis of MODE-I: Report of the MODE-I dynamics group, POLYMODE Office, MIT, 250 pp.
- Orlanski, I., and M. D. Cox, 1973: Baroclinic instability in ocean currents. *Geophys. Fluid Dyn.*, **4**, 297-332.
- Owens, W. B., and F. Bretherton, 1977: A numerical study of mid-ocean mesoscale eddies. Submitted for publication.
- Rhines, P. B., 1976: The dynamics of unsteady currents. *The Sea*, Vol. 6, E. D. Goldberg *et al.*, Eds., Wiley (in press).
- Robinson, A. R., D. E. Harrison, Y. Mintz and A. J. Semtner, 1977: Eddies and the general circulation of an idealized oceanic gyre: A wind and thermally driven primitive equation numerical experiment. *J. Phys. Oceanogr.* (in press).
- Semtner, A. J., 1974: An oceanic general circulation model with bottom topography. Numerical Simulation of Weather and Climate, Tech. Rep. No. 9, Dept. Meteor. UCLA, 99 pp.
- Tokioka, T., 1977: Parameterization of subgrid-scale mixing based on quasigeostrophic turbulence theory. Submitted for publication.
- Weatherly, G. L., 1972: A study of the bottom boundary layer of the Florida current. *J. Phys. Oceanogr.*, **2**, 54-72.
- Williams, G. P., 1969: Numerical integration of the three-dimensional Navier-Stokes equations for incompressible flow. *J. Fluid Mech.*, **37**, 727-750.